AD-F300 134

AD

TECHNICAL REPORT ARBRL-TR-02443

THREE-DIMENSIONAL
OBLIQUE SHOCK DIFFRACTION
OVER A RECTANGULAR PARALLELEPIPED:
COMPUTATIONAL/EXPERIMENTAL
COMPARISON

Richard E. Lottero
John D. Wortman
Brian P. Bertrand
Clarence W. Kitchens, Jr.

November 1982

US ARMY ARMAMENT RESEARCH AND DEVELOPMENT COMMAND
BALLISTIC RESEARCH LABORATORY
ABERDEEN PROVING GROUND, MARYLAND

DTIC
ELECTE
DEC 10 1982
S D

D

82 11 29 026

REPORT DOCUMENTATION PAGE		READ INSTRUCTIONS BEFORE COMPLETING FORM
1. REPORT NUMBER Technical Report ARBRL-TR- 02443	2. GOVT ACCESSION NO. AD-A122 254	3. RECIPIENT'S CATALOG NUMBER
4. TITLE (and Subtitle) Three-Dimensional Oblique Shock Diffraction Over a Rectangular Parallelepiped: Computational/ Experimental Comparison		5. TYPE OF REPORT & PERIOD COVERED Final Report June 79 - January 82
		6. PERFORMING ORG. REPORT NUMBER
7. AUTHOR(s) Richard E. Lottero, John D. Wortman, Brian P. Bertrand, and Clarence W. Kitchens, Jr.		8. CONTRACT OR GRANT NUMBER(s)
9. PERFORMING ORGANIZATION NAME AND ADDRESS USA Ballistic Research Laboratory ATTN: DRDAR-BLT Aberdeen Proving Ground, MD 21005		10. PROGRAM ELEMENT, PROJECT, TASK AREA & WORK UNIT NUMBERS 1L162618AH80 1L162618AH25
11. CONTROLLING OFFICE NAME AND ADDRESS US Army Armament Research and Development Command US Army Ballistic Research Laboratory (DRDAR-BL) Aberdeen Proving Ground, MD 21005		12. REPORT DATE November 1982
		13. NUMBER OF PAGES 68
14. MONITORING AGENCY NAME & ADDRESS(If different from Controlling Office)		15. SECURITY CLASS. (of this report) UNCLASSIFIED
		15a. DECLASSIFICATION/DOWNGRADING SCHEDULE

16. DISTRIBUTION STATEMENT (of this Report)

Approved for public release; distribution unlimited.

17. DISTRIBUTION STATEMENT (of the abstract entered in Block 20, if different from Report)

18. SUPPLEMENTARY NOTES

19. KEY WORDS (Continue on reverse side if necessary and identify by block number)

Oblique shock	HULL hydrocode
Shock Diffraction	Mach reflection
Finite difference	Three-dimensional
Hydrocode	Unsteady flow
S-280 shelter	Blast loading

20. ABSTRACT (Continue on reverse side if necessary and identify by block number)

Three-dimensional, unsteady finite-difference calculations with the HULL hydrocode are used to describe the shock diffraction process resulting from a shock wave striking the front of a scaled model of an S-280 Electrical Equipment Shelter at oblique incidence. The 52.5 degree obliquity of the incident 34.5 kPa (5 psi) overpressure shock on the front face produces a peak reflected overpressure that is approximately 50 percent larger than that for normal reflection. The numerical calculations are discussed and evaluated by comparison with experimental pressure measurements taken in shock tube tests on a

DD FORM 1473 EDITION OF 1 NOV 65 IS OBSOLETE

scale-model shelter. Difficulties are experienced in both the 3-D calculations and the experiment in resolving the peak reflected overpressure on the front face. Except for some disagreement in the values for peak overpressure on the shelter front and windward side faces, the comparisons between computed and experimentally measured pressure for all faces show good agreement. Three-dimensional and two-dimensional cell-size convergence studies are discussed which quantify the influence of cell size on the numerical results.

Accession For		
NTIS GRA&I	☒	
DTIC TAB	☐	
Unannounced	☐	
Justification		
By		
Distribution/		
Availability Codes		
Dist	Avail and/or Special	
A		

DTIC
COPY
INSPECTED
2

TABLE OF CONTENTS

LIST OF FIGURES

LIST OF TABLES

I. INTRODUCTION

A. Objectives

This study had two objectives. The first was to assess the ability of the three-dimensional (3-D) HULL[1,2] hydrocode to accurately predict shock diffraction loading on all faces of a rectangular parallelepiped for shock strengths of interest in the study of the airblast vulnerability of tactical equipment. A second objective was to provide further quantification of the enhancement in reflected overpressure that can occur for a shock with an overpressure ≤ 140 kPa (20.3 psi) when it strikes a target at an angle of obliquity[3-6] (typically near 45 degrees). It is important from a vulnerability viewpoint to determine whether or not such an enhanced peak can have a sufficient duration and spatial extent that a target struck at obliquity is more vulnerable than one struck at normal incidence.

A combined experimental and computational research program was undertaken at the Ballistic Research Laboratory (BRL) to provide these assessments. This report documents the first phase of the program.

B. Background

It has generally been assumed that the most severe shock loading situation for a given structure occurs when the shock strikes its most vulnerable face at normal incidence. However, when a shock wave with an overpressure ≤ 140 kPa strikes a target at oblique incidence, the peak reflected overpressure can be higher than that for normal reflection.[3-6] This oblique

---

[1] N. A. Fry, R. E. Durrett, G. P. Ganong, D. A. Matuska, M. D. Stucker, B. S. Chambers, C. E. Needham, and C. D. Westmoreland, "The HULL Hydrodynamics Computer Code," AFWL-TR-76-183, US Air Force Weapons Laboratory, Kirtland Air Force Base, NM, September 1976. (AD #B014070L)

[2] N. A. Fry, C. E. Needham, M. Stucker, B. S. Chambers, III, and G. P. Ganong, "AFWL HULL Calculations of Air Blast Over a Dam Slope," AFWL-TR-76-154, US Air Force Weapons Laboratory, Kirtland Air Force Base, NM, October 1976. (AD #B016329L)

[3] J. von Neumann, "Oblique Reflection of Shocks," Bureau of Ordnance Explosive Research, Report 12, 1943.

[4] H. Polacheck and R. J. Seeger, "Regular Reflection of Shocks in Ideal Gases," Bureau of Ordnance Explosives Research, Report 13, 1944.

[5] L. G. Smith, "Photographic Investigation of the Reflection of Plane Shocks in Air," Office of Scientific Research and Development, Report 6271, 1945.

[6] B. P. Bertrand, "Measurements of Weak Shock Wave Reflected Pressure Histories on a 2-Dimensional Surface," ABRL-MR-02966, US Army Ballistic Research Laboratory, Aberdeen Proving Ground, MD October 1979. (AD #A080539)

interaction process is of interest from both fluid dynamic and vulnerability viewpoints. Both the duration and magnitude of the peak reflected overpressures are functions of the incident shock overpressure and the angle of incidence between the shock wave and the target face. The duration is also a function of the distance along the target face, measured from the leading edge. When the angle of incidence is α_M, the angle at which Mach reflection begins,

the reflected overpressure reaches its highest possible value. For relatively small targets, the enhanced peak reflected overpressure is difficult to measure experimentally because of its small spatial extent and short time duration, and the response limitations of pressure gages. The peak reflected overpressure is difficult to predict with a finite-difference hydrodynamic computer code because of the general tendency of such codes, especially Eulerian codes, to smear discontinuities such as the incident and reflected shock waves.

The peak overpressure enhancement at obliquity for shock waves with an overpressure ≤ 140 kPa is of interest because such shock waves cover a large part of the assumed threat range from tactical nuclear weapons. The S-280 Electrical Equipment Shelter (henceforth called the shelter) houses communications equipment for many Army systems, and will be on the tactical battlefield in large numbers. The shelter is currently being hardened to decrease its blast/thermal vulnerability. A 34.5 kPa (5.0 psi) overpressure shock wave was chosen for the present work because it represents a mid-range threat level. At normal incidence, the peak reflected overpressure for this shock wave is 78.5 kPa (11.4 psi). Mach reflection for a 34.5 kPa shock wave begins at 52.5 degrees obliquity. At that angle, the peak reflected overpressure is estimated[6] to be as high as 122 kPa (17.7 psi), 55 percent greater than the value for normal incidence.

C. Topics Discussed

A brief introduction to the principal features of oblique shock diffraction is provided, with particular emphasis on the circumstances under which the peak reflected overpressure can exceed that for normal reflection. The experiments performed are described, including the facility, the model, pressure gage types and locations, and the shock and ambient conditions. The matching hydrodynamic computer code computations are also described, including detailed descriptions of the computational grids used.

In this report, the computational and experimental results for overpressure are compared at representative points on each face of the shelter model. Detailed analyses of these results are included in the presentation of the data for each face. As the experiments and computations progressed, it became apparent that neither the hydrocode computations nor the experiments were producing computed or measured overpressure peaks as high as expected. The study was then broadened to include a grid-resolution/convergence analysis with the hydrocode, and a gage-diameter/frequency-response analysis with the experiments. The results of this study are also presented.

10

II. OBLIQUE SHOCK DIFFRACTION

A. Principal Features

When an incident shock wave strikes a given face of a rectangular parallelepiped at some oblique angle, it also strikes another face at the complement of that angle. The initial contact between the incident shock wave and the structure occurs at the corner formed by the intersection of these two faces. This corner becomes a shock diffraction corner.

As the divided incident shock travels along the two perpendicular faces, rarefaction waves emanating from the diffraction corner travel along the faces at the local speed of sound relative to the moving gas. Depending on the angle of incidence of the shock on the face, the leading edge of the rare-faction wave will either fall continually farther behind the incident shock/surface intersection point, or it will travel coincident with it. The initial reflected overpressure experienced at a given point on the surface is not relieved until the corner rarefaction wave arrives, or similar waves arrive from other parts of the flow field. When the rarefaction wave is traveling coincident with the shock/surface intersection point, the reflected overpressure is relieved immediately. In the absence of viscous effects, this results in a pressure peak of vanishingly small spatial extent and duration. A more detailed discussion of oblique shock diffraction may be found in Appendix A.

B. Reflected Shock Enhancement

The incident shock wave of interest here is a 34.5 kPa overpressure shock. Figure 1 shows the shock reflection factor (the ratio of the peak reflected overpressure to the incident overpressure) as a function of the angle of shock incidence, α, for this shock strength. Regular reflection theory is valid for $0 \leq \alpha \leq \alpha_C$. This angle, α_C, is the smallest angle at which the corner rare-faction wave travels coincident with the incident shock/surface intersection point. The experimental data indicate that the peak overpressure is reached at $\alpha_N = 52.5$ degrees. At that angle, α_N, the intersection point between the incident and reflected shocks is on the verge of lifting off the surface; for $\alpha > \alpha_N$ a Mach stem and triple point are formed.

Information inferred[6] by measuring the Mach stem velocity for $\alpha \sim \alpha_N$ indicates that the peak reflected overpressure behind the Mach stem may be even larger (122 kPa) than that indicated by the experimental data in Figure 1. The enhanced peak reflected pressure for $\alpha \sim \alpha_N$ is of interest from computational and experimental viewpoints, and may have important implications in blast vulnerability.
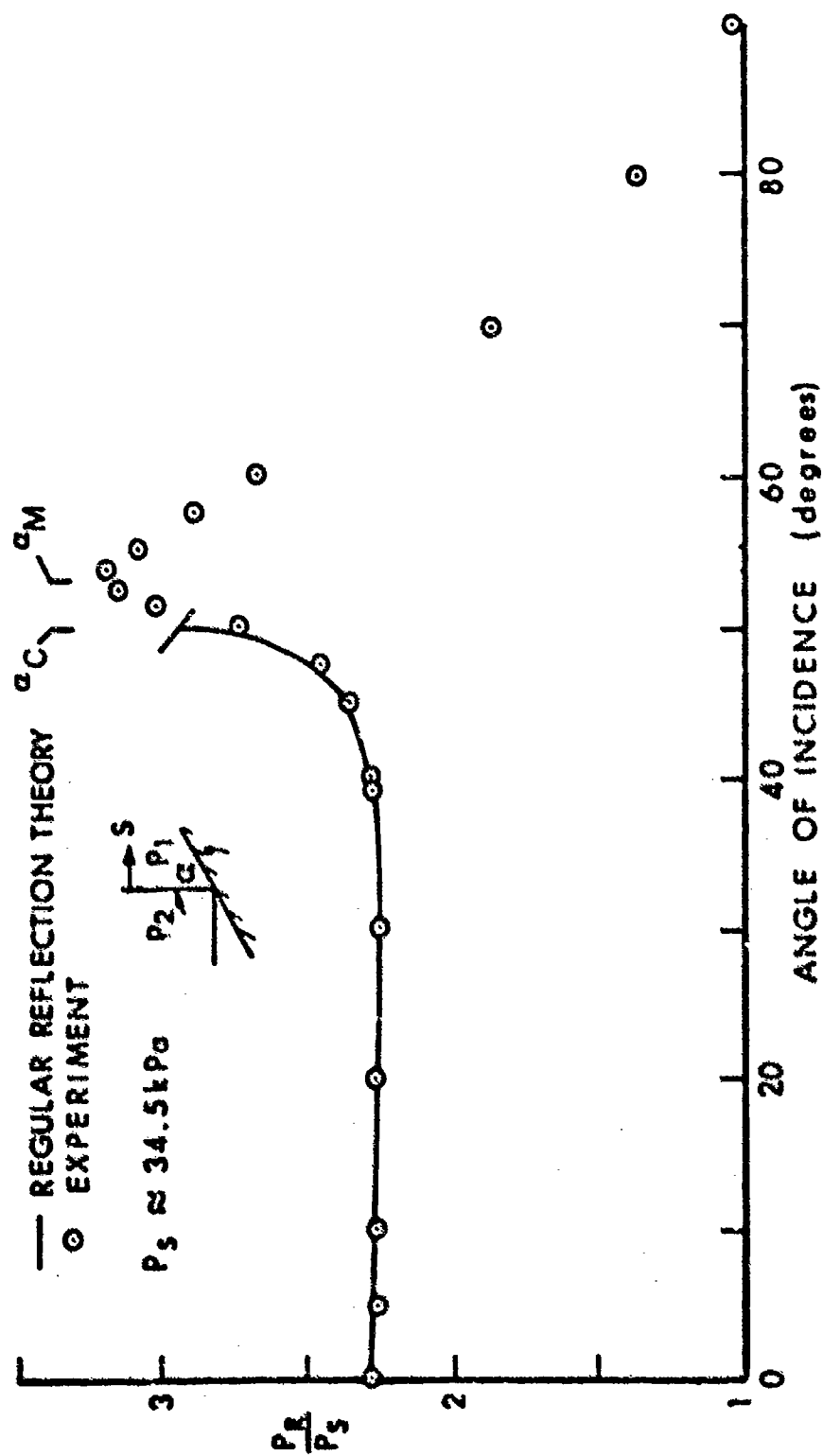
Figure 1. Variation of shock reflection factor with angle of incidence. (Reproduced in part from Reference 6)

III. EXPERIMENTS

A. Experimental Facility and Model

The experiments were conducted in the BRL 0.6 metre diameter shock tube.[7]
A non-responding 1/18.45 scale model of the shelter was constructed of aluminum,
with dimensions 19.58 cm (width) by 11.38 cm (height) by 11.79 cm (depth).
One of the 19.58 cm by 11.38 cm faces is defined as the front face. The model
was mounted in the shock tube so that the angle, α, between the front face and
the incident shock wave front was 52.5 ± 0.5 degrees. One of the 11.79 cm by
11.38 cm faces is defined as the windward side face, the angle between that
face and the incident shock being 37.5 degrees. The model produces a blockage
of 9.4 percent of the 50.8 cm by 50.8 cm test section cross-sectional area in
that orientation, based on its projected area.

B. Experiments Conducted

Airblast loading experiments were conducted for various overpressures and
angles of incidence. The two described in Table 1 will be discussed here.
The angle between the shock front and the shelter front face is α, p is
absolute pressure, T is temperature, and E.1 and E.2 are the (simplified) shot
numbers used in this report. Additional information on the experiments is
given in Appendix B.

TABLE 1. EXPERIMENTAL SHOTS

Shot Number		α	Ambient Values		Shock Overpressure
Actual	This Report	(Degrees)	p(kPa)	T($^\circ$C)	(kPa)
24-79-126	E.1	52.5	101.42	22.25	32.75
24-79-134	E.2	52.5	101.90	24.31	34.50

C. Pressure Gages

There were a total of eight pressure gages on the model, mounted flush to
the model surface. Table 2 shows the gage positions where pressure measurements
will be compared with the hydrocode computations. The gage locations are
given in a primed coordinate system, having its origin at the bottom corner
of the leading vertical edge of the model. The front and back faces are
constant X' planes, the side faces constant Y', and the top and bottom faces
constant Z'. The gage positions are defined by a letter-and-number pair; the
letter denotes the face and the number denotes the gage position on the face.

---

[7] G. A. Coulter and B. P. Bertrand, "BRL Shock Tube Facility for the
Simulation of Air Blast Effects," BRL-MR-1685, US Army Ballistic
Research Laboratory, Aberdeen Proving Ground, MD, August 1965.
(AD #475669)

All gages in shots E.1 and E.2 had a sensitive element diameter of 0.51 cm (0.20 in), except gage F2 in shot E.2, which had a smaller diameter of 0.16 cm (0.063 in) and a higher frequency response than the other gages. (Reference 8 incorrectly described the diameter of this latter gage as 0.32 cm.)

TABLE 2. GAGE POSITIONS

Gage Number	Face	X' (cm)	Y' (cm)	Z' (cm)
F2*	Front	0.00	14.68	2.84
F4	Front	0.00	4.90	8.53
B2**	Back	11.79	14.68	2.84
B4	Back	11.79	4.90	8.53
S1	Leeward Side	5.89	19.58	5.69
S2	Windward Side	5.89	0.00	5.69
T1	Top	5.89	14.68	11.38
T2	Top	5.89	4.90	11.38

*High frequency gage, shot E.2.

**No gage, shot E.2.

IV. FINITE DIFFERENCE COMPUTATIONS

A. Hydrodynamic Computer Code

The airblast version of the HULL[1,2] hydrodynamic computer code was used for the shock diffraction computations. The HULL code currently in use at the BRL is AFWL version 8, received in September 1978, with modifications made

---

[8] R. E. Lottero, J. D. Wortman, B. P. Bertrand, and C. W. Kitchens, Jr., "Oblique Interaction of a Shock Wave with a Three-Dimensional Tactical Communications Shelter," Army Research Office Report 80-3, Proceedings of the 1980 Army Numerical Analysis and Computers Conference, August 1980. (AD #A089089)

14

by the BRL, and by SAI[9] under contract to the BRL. Some of the modifications were necessary to run the code on the BRL's CDC 7600; others were necessary to convert from using a SAIL[10] preprocessor to using a CDC-UPDATE/SAI-POST preprocessing system. Other modifications were added to allow the input of an off-angle step shock through any combination of the left, bottom, and back (aft) boundaries of a 3-D computational grid and the left and bottom boundaries of a 2-D Cartesian grid.

The HULL hydrocode uses an explicit time step, predictor-corrector method similar to a Lax-Wendroff[11] scheme to solve the inviscid Euler equations. Each computational step is performed in two phases, a Lagrangian phase where flow field cells perform work on one another, and an Eulerian phase where material is fluxed across cell boundaries using a donor cell method.

B. Computations Performed

Table 3 lists the HULL hydrocode computations described in this report. Computation H.1, which matches experiment E.1 in shock strength and ambient conditions, will be discussed in detail in this and the next section. The remaining HULL computations, H.2 - H.7, match experiment E.2. Results from H.2 - H.7 will be discussed in the section titled "Convergence Study." The Courant-Friedrichs-Lewy number was 0.5 for all computations; artificial viscosity was not used.

TABLE 3. HULL HYDROCODE COMPUTATIONS

Calculation Number		Dimensions	Cell Sizes Relative to H.1	Shock Overpressure (kPa)
Actual	This Report			
37.126	H.1	3-D	1.0	32.75
37.0	H.2	3-D	1.0	34.50
37.001	H.3	3-D	0.5	34.50
37.11	H.4	2-D	1.0	34.50
37.9	H.5	2-D	0.5	34.50
37.10	H.6	2-D	0.25	34.50
37.6	H.7	2-D	0.125	34.50

[9] J. A. Hoedal, B. S. Chambers, and R. W. Clemens, "Support to BRL: HULL Code Implementation on a CDC 7600," SAI-80-701-AQ, Science Applications, Inc., McLean, VA, August 1979.

[10] D. C. Graham, L. P. Gaby, and C. E. Rhodes, "SAIL, An Automated Approach to Software Development and Management," AFWL Interim Report 1971-6, US Air Force Weapons Laboratory, Kirtland Air Force Base, NM, October 1976.

[11] R. D. Richtmyer and K. W. Morton, Difference Methods for Initial Value Problems, Interscience Publishers, Inc., John Wiley & Sons, Inc., Second Edition, 1967.

C. Finite Difference Grids

The finite difference grid used for computation H.1 contains 92,512 flow field cells, with a 49 × 59 × 32 grid in the X, Y, and Z directions, respectively. The shelter is modeled using 6,912 nearly cubical rigid cells, with 16 equal X-direction cells ($\Delta X = 0.7366$ cm), 27 equal Y-direction cells ($\Delta Y = 0.7253$ cm), and 16 equal Z-direction cells ($\Delta Z = 0.7112$ cm). The rigid cells do not directly enter the computation, but they do require the same storage space as a hydrodynamic cell, so this space is wasted. To minimize the smearing of the computational shock as it passes through the grid prior to striking the shelter, the shock is placed well into the grid at the initiation of the computation, 2.66 cm upstream from the shelter leading edge. The shock input algorithm keeps track of the theoretical intersection of the shock wave with the computational boundaries, progressively moving the input shock along the boundaries as the computation proceeds.

Appendix C contains detailed descriptions of the computational grids used in this study.

D. The Flow Field

Figure 2 shows a top view of an isobar (constant pressure) plot of the flow field for H.1 in the bottom-most plane of cells after one computational cycle. (A similar plot is not available at cycle 0.) Shock arrival time at the shelter leading edge is defined as t = 0.0. In Figure 2, the incident computational shock is indicated by the closely-spaced pressure contours. (The apparent excessive width of the shock is an artifact of the contour-plotting algorithm.) The shock is moving from the lower left corner of the figure toward the upper right corner. What appears to be a bent right end of the shock is actually the set of pressure contour indentification numbers which are overwritten by the plot routine. The contour labelled "1" is not a pressure contour, but is an artificial use of the contour algorithm to show the outline of the shelter in this plane.

Figure 3 shows isobars in the same plane at t = 374.9 µs; the shock wave has passed slightly more than half-way across the shelter. Contour 5 shows the general shape of the reflected shock. Figures 2 and 3 give a qualitative indication of the flow field predicted by the 3-D HULL hydrocode. The next section provides detailed comparisons between experiment E.1 and HULL computation H.1.

V. COMPARISON OF COMPUTATIONAL AND EXPERIMENTAL RESULTS

A. General Comments

This section shows typical comparisons between measured and computed overpressure on each face of the model. In this section, "experiment" refers to experiment E.1, and "computation" refers to computation H.1. Computation H.1 was run on the BRL CDC 7600 for 155 computational cycles, with a total job time of 49 minutes.
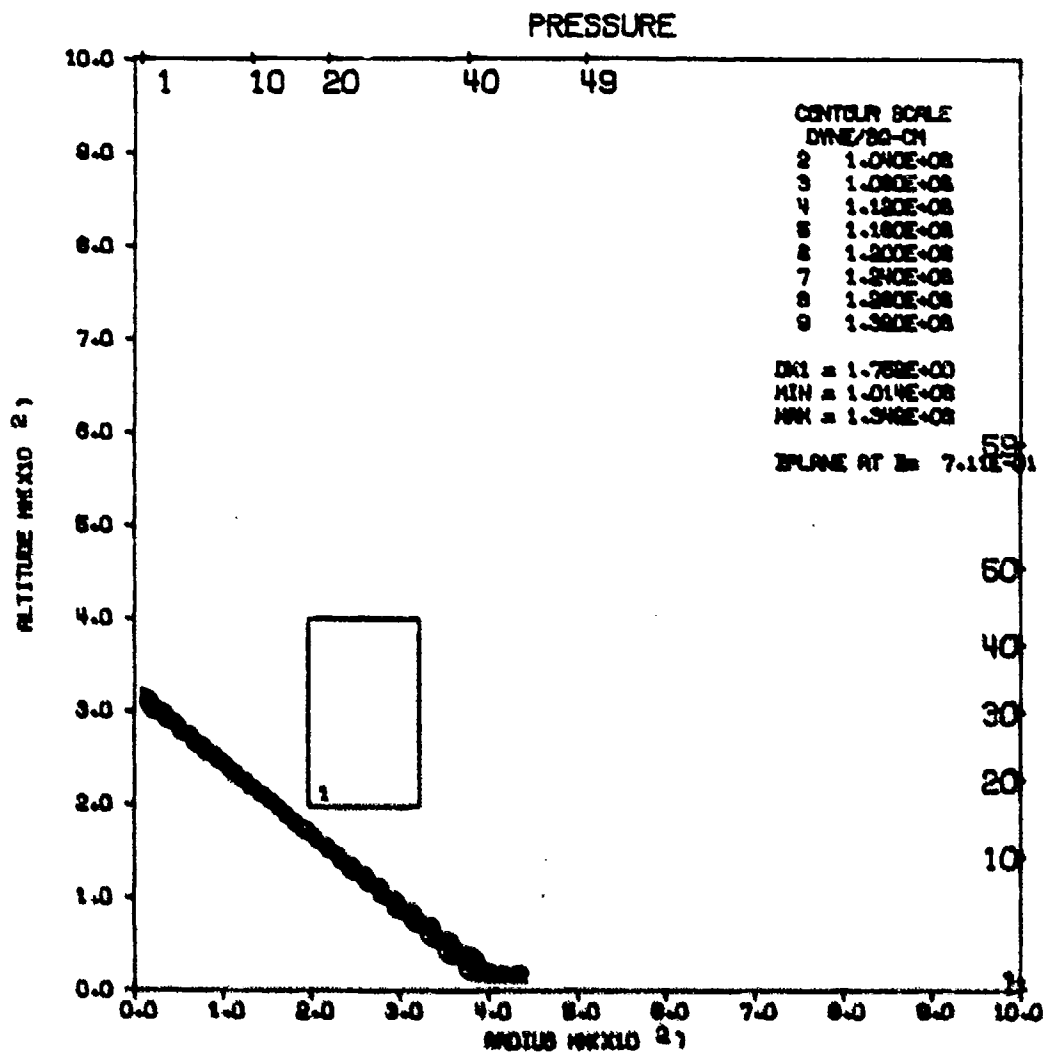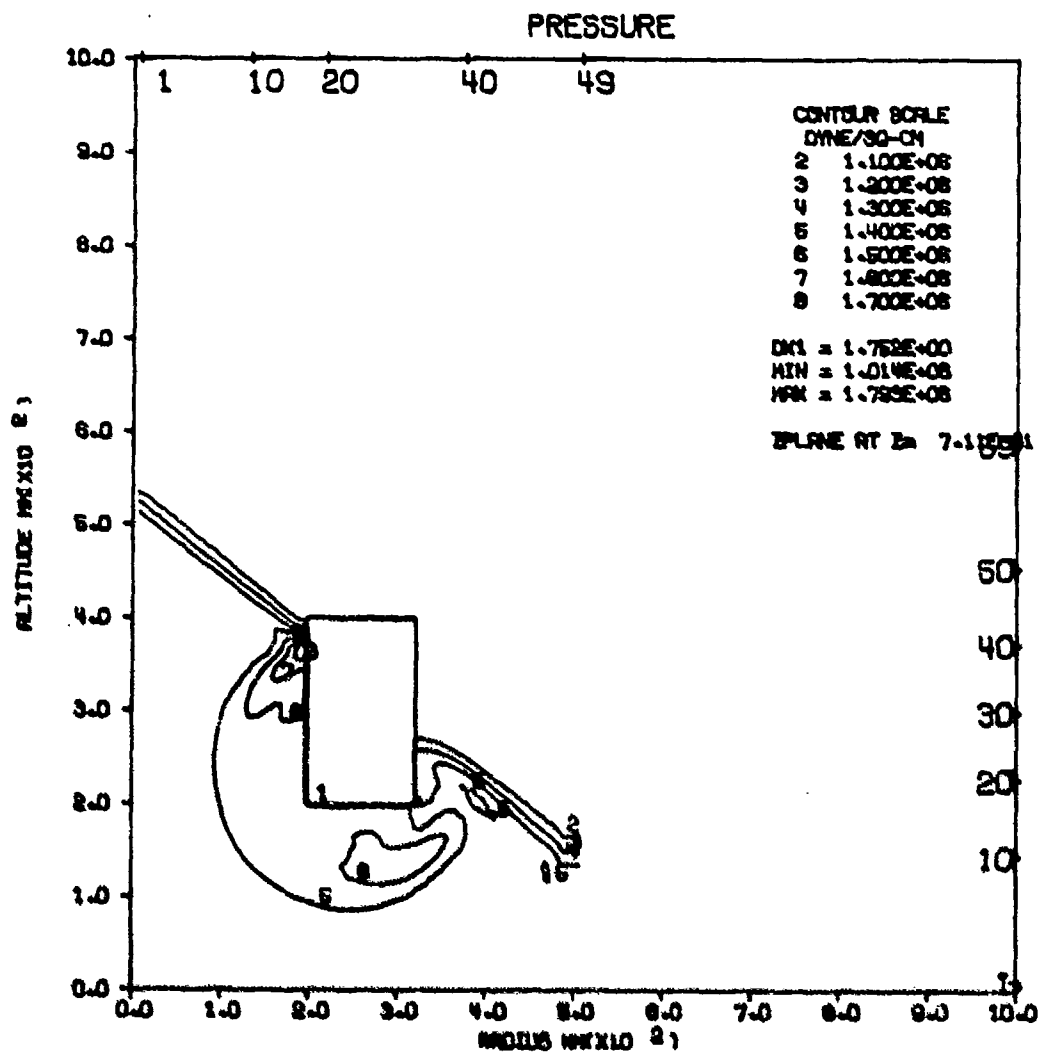
Figure 2. Isobars at t = -68.2 μs in ground plane for H.1.

17

Figure 3. Isobars at t = 374.9 μs in ground plane for H.1.

B. Front Face

Figure 4 shows a comparison between the measured and the computed overpressure vs time for gage F2. The gage is located at 3/4 of the distance along the shelter front face from the leading edge and at 1/4 of the shelter height from the ground plane. The agreement between the two results is good, except for the initial shock interaction with the structure. Because the computational shock is spread over three or four cells, it shows an earlier initial rise and a reduced peak.[12] The agreement beyond the peak is very good, although the computed overpressure is slightly greater than that for the experiment for $0.6 \leqslant t \leqslant 1.2$ ms. The second peak in the experimental data at 1.22 ms is caused by the arrival of a secondary shock produced by the interaction of the incident shock with the model; it traveled to the shock tube wall, reflected from the wall, and returned to strike the model. A similar second peak is seen in the other comparisons in this section. The X's on the H.1 curve in this and the next four figures mark every fifth computed data point; they have been added primarily as a visual aid.

Figure 4 shows a measured peak reflected overpressure of 86.2 kPa occurring at 0.320 ms, and a corresponding computed peak of 76.2 kPa at 0.331 ms. The difference in time is due in part to the difficulty in establishing a zero reference time at the leading edge of the shelter for the experiment because of the discrete data sampling rate and the gage diameter and response time. Time zero was deduced from the experimental data using the incident shock speed and the time at which a reference gage on the model first sensed a pressure signal above a threshold value. This was taken to indicate shock arrival at the gage, but this method has some inherent uncertainties. The experimental wave speed was computed by using the measured pressure jump across the incident shock wave. The wave speed thus computed for E.1 was 389.3 m/s. The data for E.1 were sampled at 2.5 µs intervals. The diameter of the gage was 0.51 cm, so it took the incident shock 13.1 µs or 5.24 sampling counts to traverse the gage. The time difference in the peaks for E.1 and H.1 for F.2 was 11 µs, which is within one digital sampling count of the 13.1 µs shock traversal time across the gage.

There was also an inherent error in the time of peak overpressure computed by the HULL hydrocode. The numerical diffusion of the shock wave as it travels through the finite difference grid has been demonstrated [12-14] to cause a

---

[12] R. E. Lottero, "Comparison of 3-D Hydrocode Computations for Shock Diffraction Loading on an S-280 Electrical Equipment Shelter," Army Research Office Report 80-3, Proceedings of the 1980 Army Numerical Analysis and Computers Conference, August 1980. (AD #A089089)

[13] R. E. Lottero, "A Detailed Comparison of 3-D Hydrocode Computations for Shock Diffraction Loading of an S-280 Electrical Equipment Shelter," ARBRL-TR-02334, US Army Ballistic Research Laboratory, Aberdeen Proving Ground, MD, June 1981. (AD #A1c3613)

[14] R. A. Gentry, L. R. Stein, and C. W. Hirt, "Three-Dimensional Computer Analysis of Shock Loads on a Simple Structure," BRL-CR-219, US Army Ballistic Research Laboratory, Aberdeen Proving Ground, MD, March 1975. (AD #B003208L)
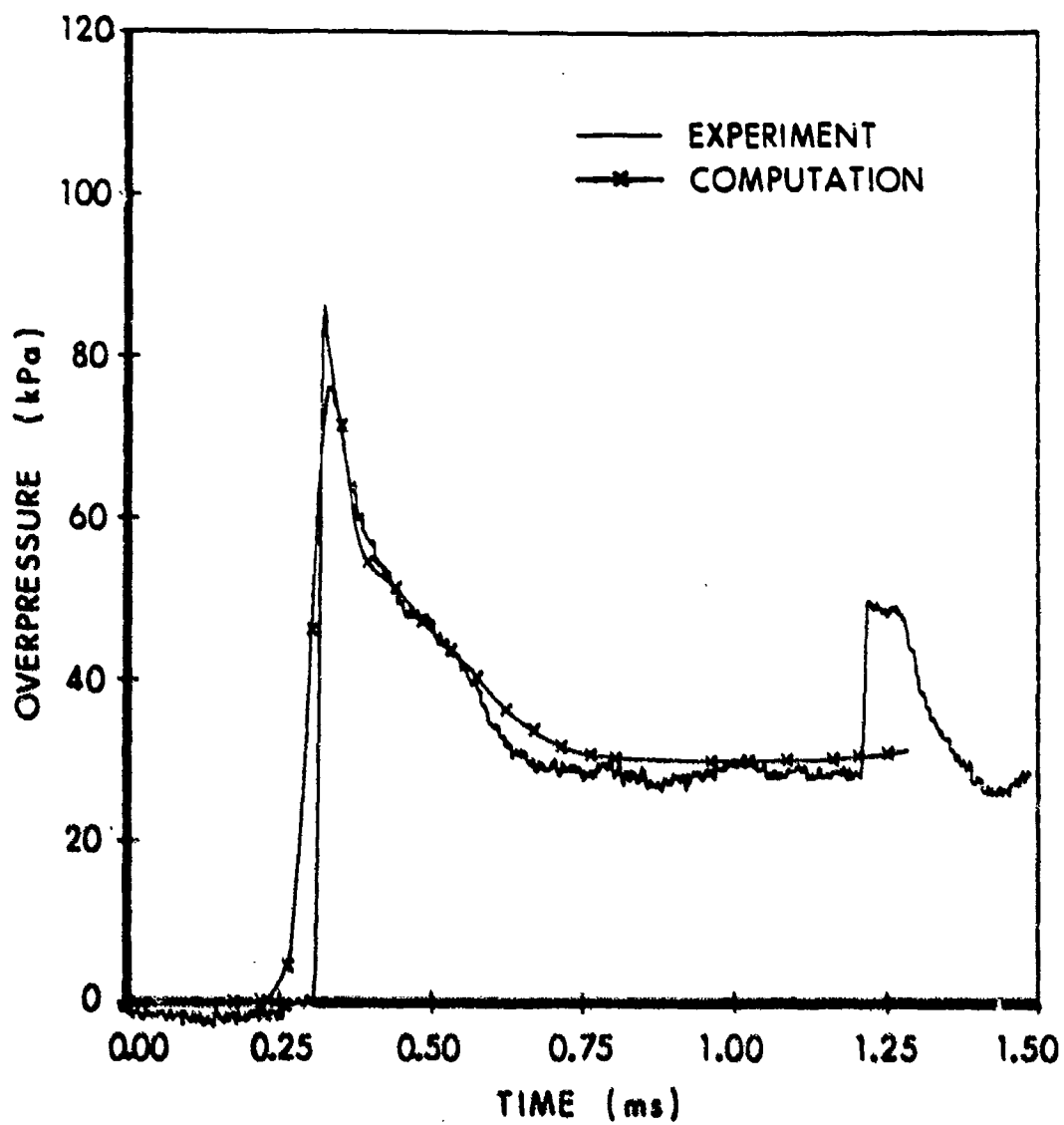
Figure 4. Comparison of measured and predicted overpressure
on front face gage F2.

delayed and reduced peak reflected overpressure when the shock interacts with a structure. Thus, each method contributed to the uncertainty in establishing a common reference time. It was decided to establish time-zero estimates for the experiment and the computation independently and use these to compare the results, rather than arbitrarily shift the overpressure curves in time to get a more pleasing visual alignment.

Neither the measured nor the computed peak reflected overpressure were near the expected peak of 115 kPa (see the section entitled "Convergence Study"). The measured peak of 86.2 kPa is 25 percent less than the expected peak, and 16 percent greater than the peak for normal reflection. The computed peak is 34 percent less than the expected peak, and 3 percent greater than the peak for normal reflection. This is most likely due to the finite gage and cell sizes which are used. In the experiment, the gage diameter is 2.6 percent of the span of the front face. In the computation, the cell dimension in the Y direction on the front face is 42 percent larger than the gage diameter and 3.7 percent of the span. It appears that the spatial extent of the over-pressure peak is so small that it is largely integrated out, even with these relatively small units of measure. Thus, it can be concluded that the over-pressure peak does not make a significant contribution to the loading on the model and hence is probably not significant to the shelter itself. The problem of resolving the peak is still of interest from a fluid dynamics viewpoint, and will be discussed further in the section entitled "Convergence Study."

Analysis of the experimental data shows that gage F2 recorded a higher peak reflected overpressure (86.2 kPa) than did gage F4 (73.8 kPa). This is because gage F2 was farther from the leading edge than was gage F4, and so the pressure peak had more opportunity to develop spatially, as discussed in Appendix A. (Data for gage position F4 are not shown here.)

C. Windward Side Face

Figure 5 shows a comparison between the measured and computed overpressure histories for gage S2, located in the center of the windward side face. The angle between the shock front and this face is 37.5 degrees. The agreement is good except for the initial shock interaction. For this angle, the expected peak reflected overpressure (see Figure 1) is essentially equal to the normal reflection overpressure of 74.2 kPa. The computational peak is 77.8 kPa, 5 percent greater than the normal reflection value and 7 percent greater than the measured peak (73.0 kPa), which is in turn 2 percent lower than the normal reflection peak. The peak values for this gage position will be discussed further in the section entitled "Convergence Study."

D. Leeward Side Face

Figure 6 shows a similar comparison for gage S1, located at the center of the leeward side face. It, too, shows a smearing of the computational shock, which has also been weakened by a rarefaction wave produced at the trailing edge of the front face. The general agreement between the curves is good. They both show a pressure plateau of 22.5 kPa for $0.6 \leqslant t \leqslant 0.9$ ms, caused by the weakened incident shock. The pressure rise which begins at 0.9 ms is caused by the incident shock breaking over the top face, sending another
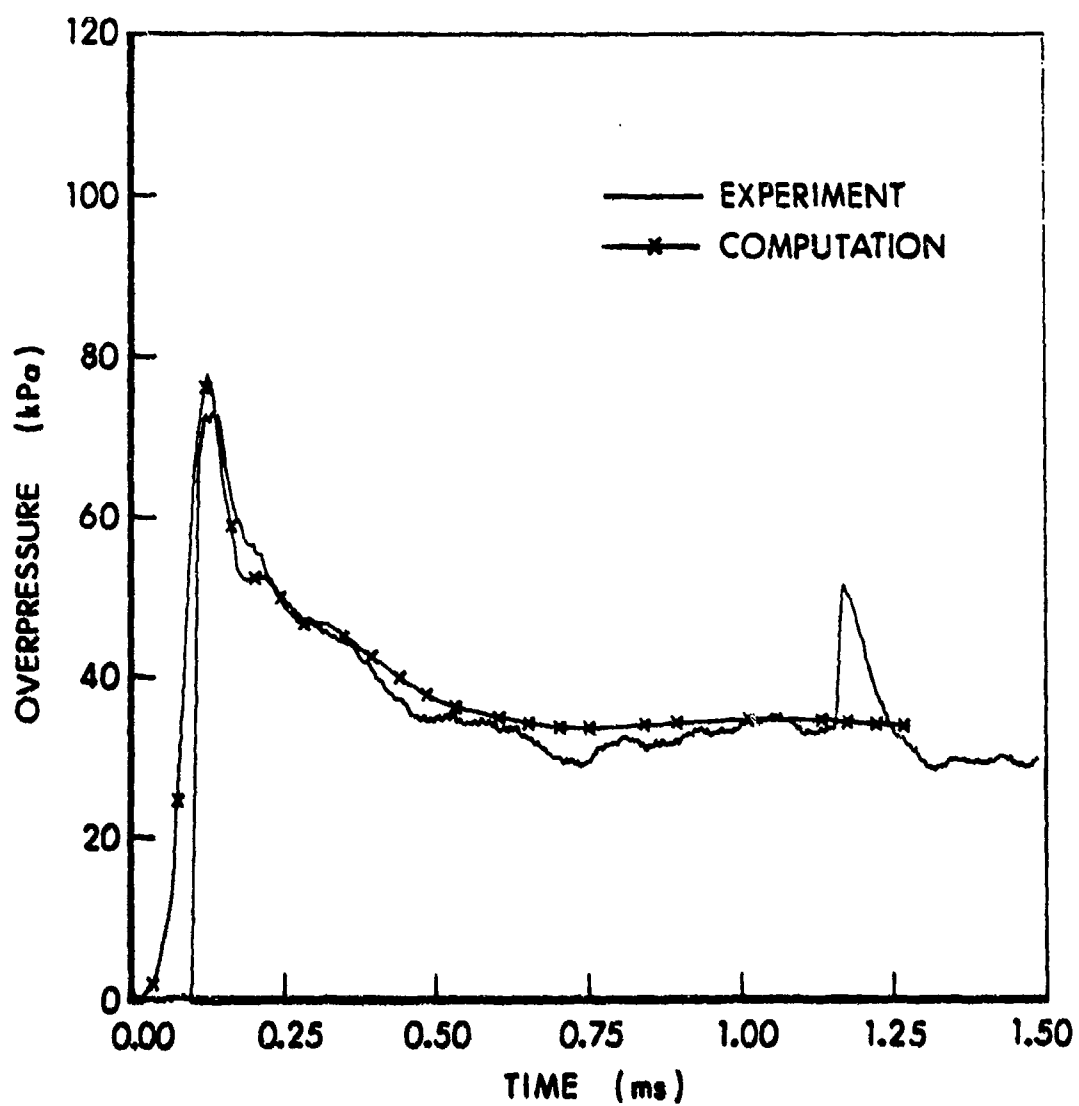
21

Figure 5. Comparison of measured and predicted overpressure on windward side face gage S2.

22
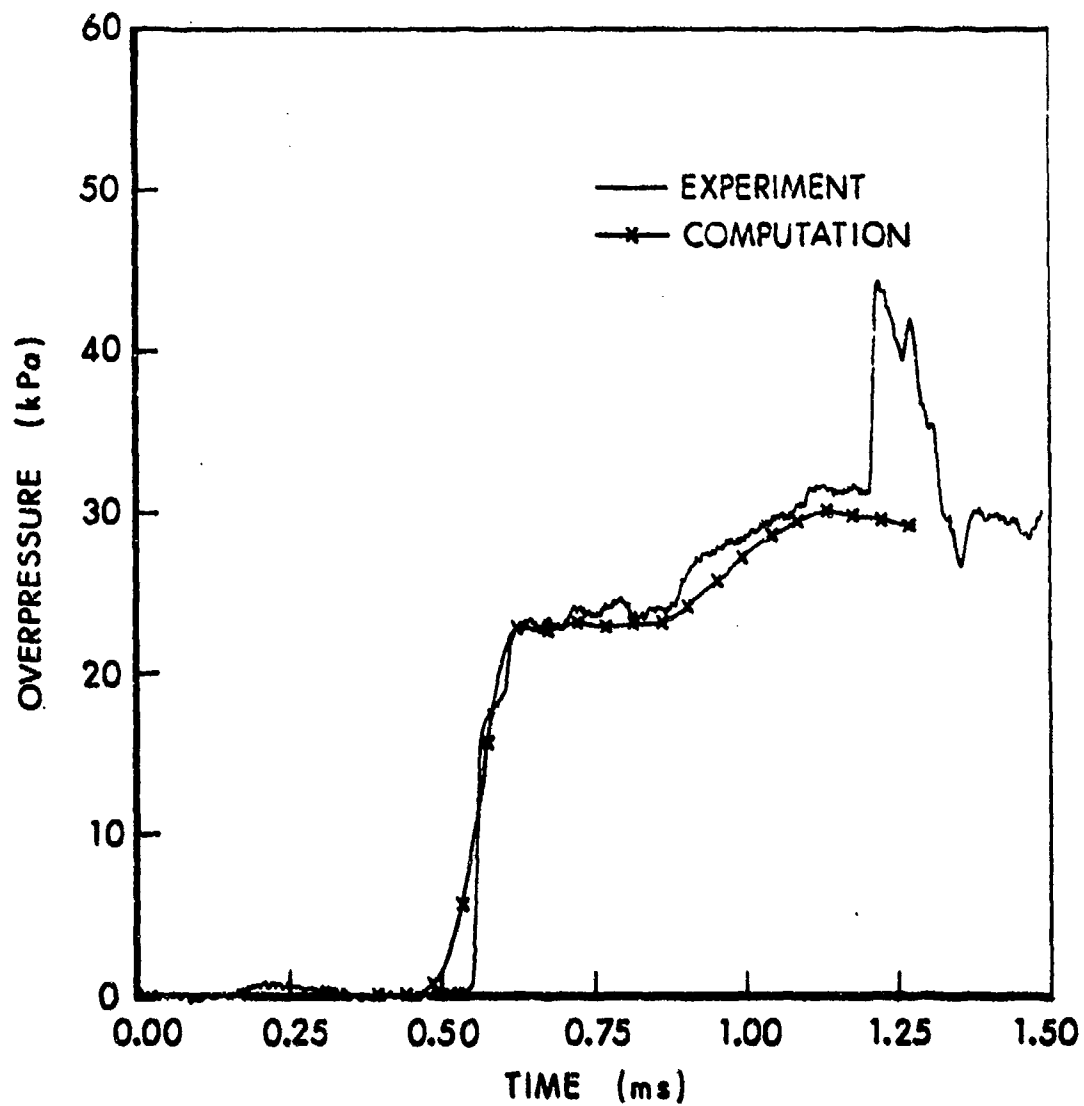
Figure 6. Comparison of measured and predicted overpressure on leeward side face gage S1.

weakened shock down the leeward side face. The curves agree qualitatively,
but the computed results vary from 5 to 10 percent less than the experimental
results after 0.9 ms. It may be that viscous effects, which HULL cannot model,
are becoming important by this time.

E. Back Face

Figure 7 shows a similar comparison for back face gage B2. This gage is
located at 3/4 of the distance along the back face, and 1/4 of the height of
the shelter from the ground plane. The agreement between the computed and
the measured results is very good, except at the time of initial shock arrival
and for t > 1.0 ms.

F. Top Face

Figure 8 shows a comparison between the measured and computed overpressure
histories for gage T2, located on the top face (see Table 2). Except for the
overpressure peaks, the agreement between the computation and experiment is
good, with the computed pressure consistently larger. The computed overpressure
peak of 39.5 kPa at 0.22 ms is 18 percent greater than the experimental peak
of 33.4 kPa at 0.20 ms. The HULL result for the overpressure peak is the
value in error; this is possibly related to a numerical overshoot associated
with the top corner of the shelter. The comparison plot for top face gage T1
(not shown here) shows similar behavior.

VI. CONVERGENCE STUDY

A. Reason for Study

Because the expected peak reflected overpressure was not obtained on the
front face (gage position F2) in either the calculations or the experiment,
a convergence study was performed to study the sensitivity of the peak values
to both cell and gage size. It was expected that smaller cell sizes and smaller
gages having higher frequency response were needed to resolve the small region
of enhanced reflected overpressure on the front face.

B. Computations and Experiments

Only a limited grid refinement was possible for the 3-D computational
problem because of cost and storage limitations. Most of the computational
results were obtained for a representative 2-D slice of the grid for H.1, which
then modeled a shelter with infinite height. Experiment E.2 was performed to
study the effect of reduced gage size and higher frequency response on the
measured front face peak.

The cell-size convergence study matching shot E.2 consisted of two 3-D
computations, H.2 and H.3, and four 2-D computations, H.4 - H.7 (see Table 3).
The relative cell sizes in Table 3 were computed by dividing the cell sizes
for the particular grid by the respective values of ΔX, ΔY, and ΔZ on the
shelter surface for H.1. The experimental gage sizes are scaled in the same
way, using ΔY from H.1 for the front face gage and ΔX from H.1 for the
windward side gage.

24

Figure 7. Comparison of measured and predicted overpressure on back face gage B2.

Figure 8. Comparison of measured and predicted overpressure on top face gage T2.

C. Results

1. Front Face.

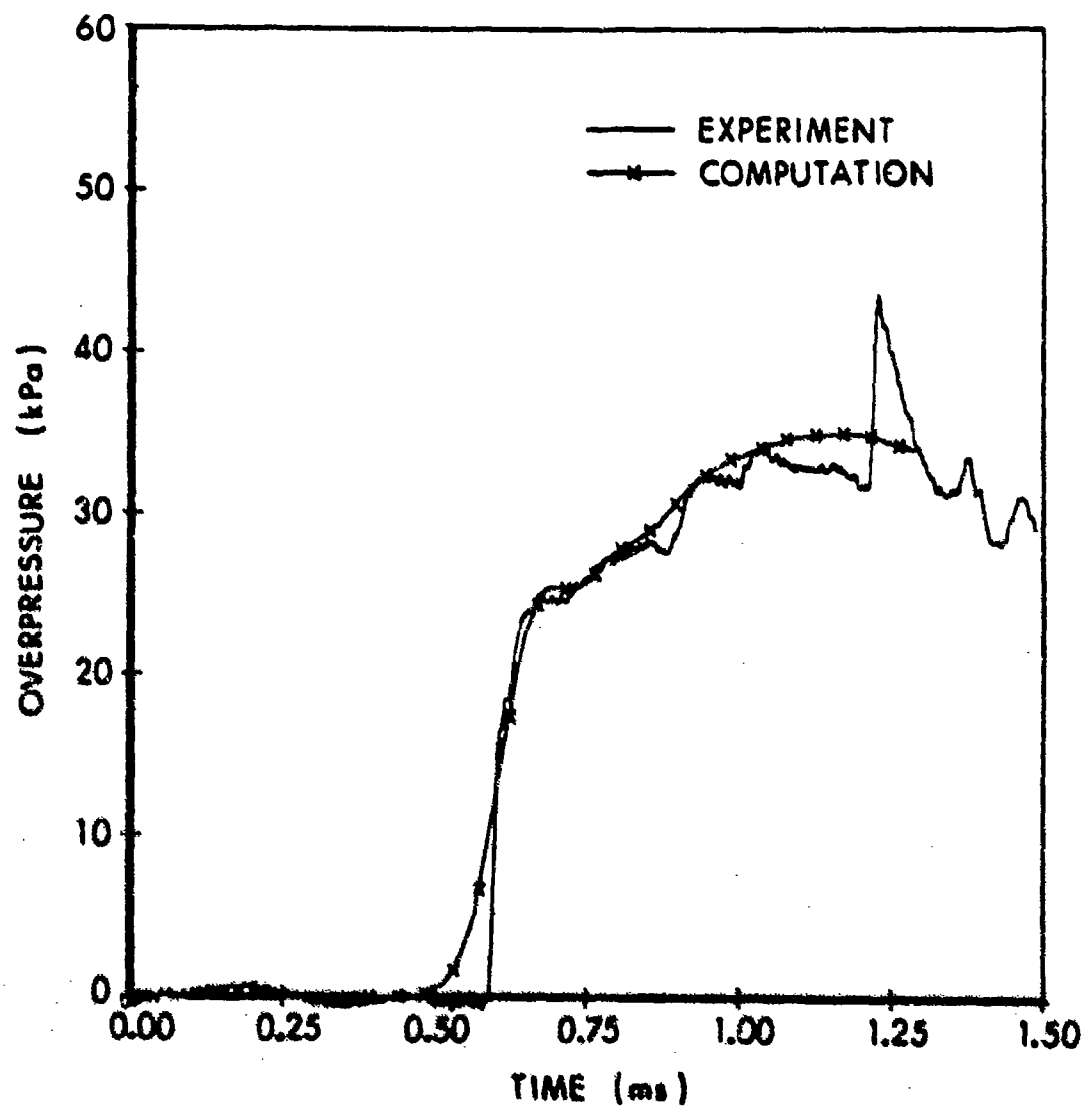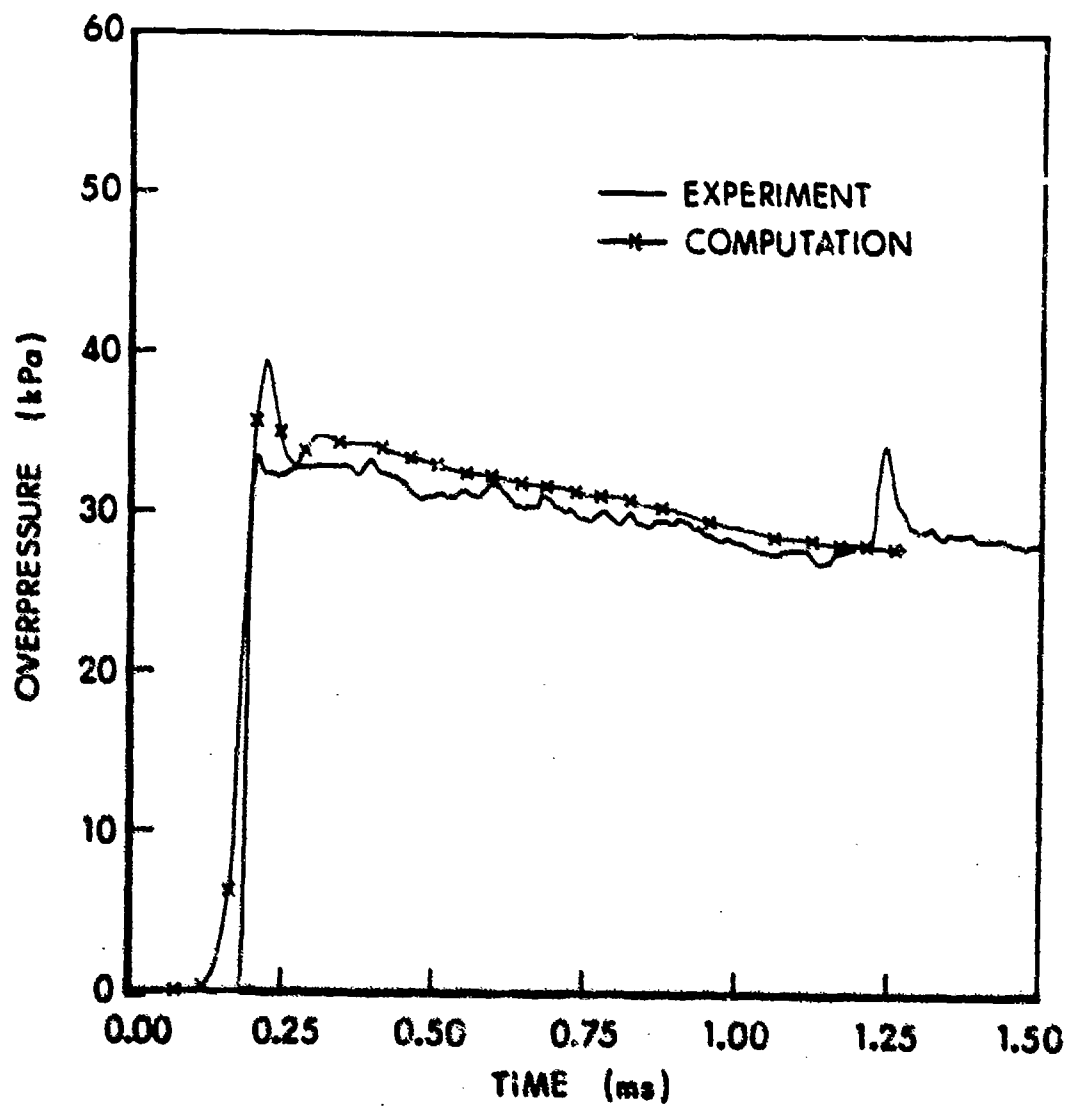Figure 9 shows a comparison of the peak reflected overpressures obtained at gage position F2 on the front face. Neither the experimental (E.1) nor the computed (H.1) values were near the expected peak of 115 kPa for that 32.75 kPa shock.* The experimentally measured peak of 86.2 kPa is 25 percent below the expected peak and 16 percent above the normal reflection peak of 74.2 kPa. The corresponding computed peak in H.1 is 76.2 kPa, 34 percent less than the expected peak and 3 percent greater than the normal reflection peak.

Once these comparisons were made, the problem then was to determine what could be done both experimentally and computationally to obtain peak overpressures closer to the expected values. If neither E.1 nor H.1 produced peak overpressures near 115 kPa because the measuring elements (either gages or flow field cells) were too large, then it should be possible to measure higher peaks experimentally with a smaller diameter, higher-frequency-response gage and compute higher peaks with smaller flow field cells. For E.1, the gage diameter was 0.51 cm, 2.6 percent of the span of the front face. For H.1, the cell dimension in the Y direction on the front face was 0.7253 cm, 3.7 percent of the span of the front face, and 42 percent larger than the gage diameter.

A second experiment, shot E.2, was fired with a smaller diameter (0.16 cm) higher-frequency-response gage at position F2. The experimental conditions and gages used for E.2 are summarized in Tables 1 and 2. The measured peak overpressure at gage F2 in shot E.2 was 88.6 kPa, 27 percent below the expected peak of 122 kPa, and 13 percent above the normal reflection peak of 78.5 kPa. The relative difference in measured peaks for E.1 and E.2 was within the range of experimental error, and hence inconclusive.

The diameter of the gage at position F2 for shot E.2 was 0.82 percent of the length of the front face, a reduction in gage diameter of 69 percent relative to shot E.1. Even with this relatively small high-frequency-response gage, the overpressure peak was of sufficiently short duration and limited spatial extent that it was of little significance to the loading on the shelter front face.

The computational convergence study involved several computations, both 2-D and 3-D, for a 34.5 kPa overpressure shock (see Table 3). The column in Table 3 indicating relative cell sizes is computed by taking a cell dimension on the model surface, and dividing it by the corresponding cell dimension in computation H.1. (See appendix C for additional details concerning the computational grids.) Table 4 gives a summary of the computed and measured peak overpressures at gage position F2. (These values are also plotted on Figure 9.) There is a clear trend toward increasing peak overpressure with decreasing flow -

---

* The expected peak reflected overpressure for a 34.5 kPa shock at 52.5 degrees obliquity is 122 kPa,[6] 1.55 times the normal reflection overpressure of 78.5 kPa. If a similar enhancement is assumed for the 32.75 kPa overpressure shock in E.1, then a peak reflected overpressure no higher than 115 kPa can be expected. This is because α_M > 52.5 degrees for a 32.75 kPa shock.
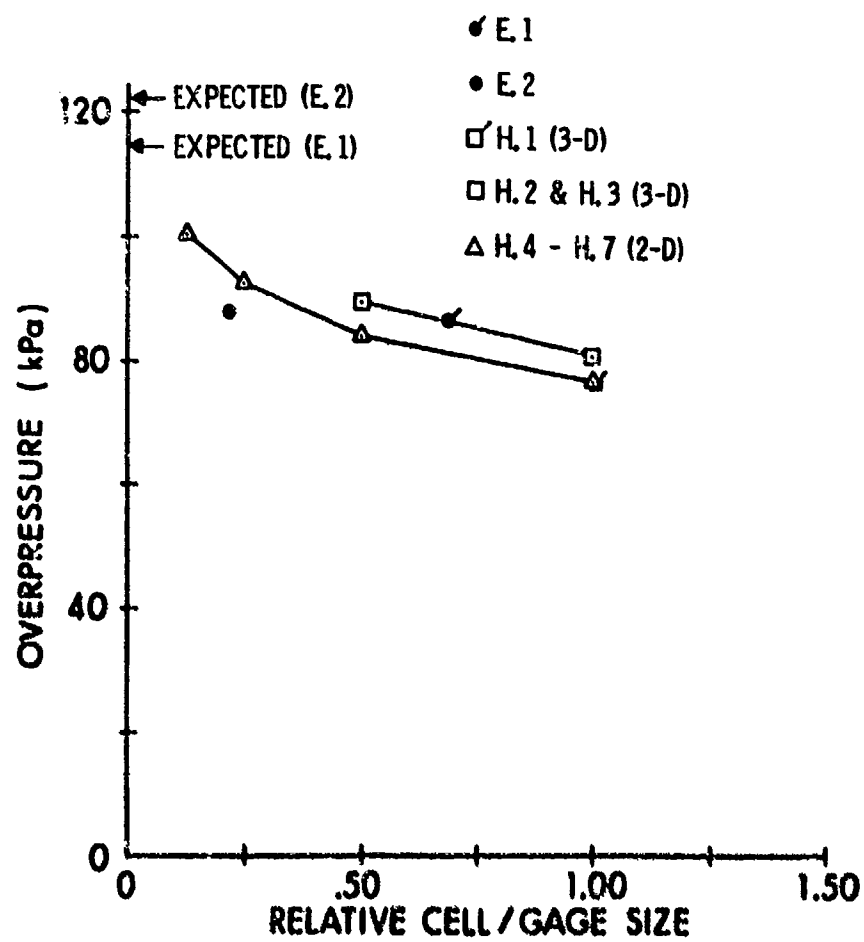
Figure 9. Peak overpressure at front face gage position F2.

field cell size. However, because of the rapidly increasing cost of the computations as the cell size was decreased, it was not possible to determine whether the computed peak would approach the expected value asymptotically as cell size was decreased further, approach some other value, or increase without bound.

TABLE 4. PEAK OVERPRESSURE, GAGE F2

Source	Peak Overpressure (kPa)	Peak/NRP*	Peak/IP**
E.1	86.2	1.16	.75
H.1	76.2	1.30	.66
E.2	88.6	1.13	.73
H.2	80.4	1.02	.66
H.3	89.4	1.14	.73
H.4	76.5	.97	.63
H.5	83.9	1.07	.69
H.6	92.2	1.17	.76
H.7	100.4	1.28	.82

*NRP = Theoretical normal reflection peak overpressure, 74.2 kPa for the 32.75 kPa overpressure shock, and 78.5 kPa for the 34.5 kPa overpressure shock.

**IP = Inferred peak at α_M, 115 kPa for the 32.75 kPa overpressure shock, and 122 kPa for the 34.5 kPa overpressure shock.

There was one other interesting feature noted in this convergence study, not directly related to the problem at hand. There is a systematic displacement between the 2-D and 3-D results for identical shock and ambient conditions, apparently due to differences in the finite difference algorithms in the two versions of the HULL code.

2. Windward Side Face.

Figure 10 shows the results of the convergence study for gage position S2. In this case, α = 37.5 degrees, and the expected peak overpressures are the same as for normal reflection. The qualitative trend is similar to
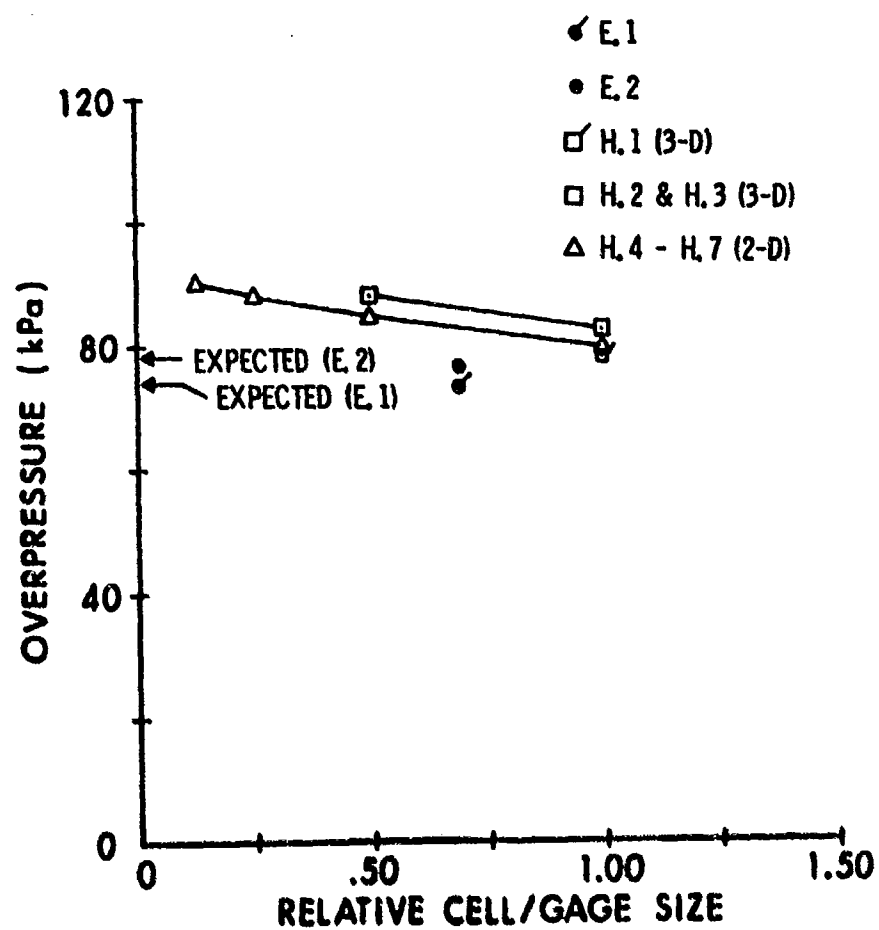
Figure 10. Peak overpressure at windward side face gage position S2.

that shown in Figure 9. The computational results overshoot the expected
values by as much as 20 percent as the cell size is decreased, indicating an
artificial sensitivity of the peak value to cell size.

In this study, the computed peak rises monotonically with decreasing
cell size for both the front and windward-side faces. This sensitivity to
grid size has also been documented by Carpenter et al.[15] for strong shocks
(pressure ratio > 20), but the relation there was nonmonotonic.

VII. CONCLUSION

This study has shown that the 3-D HULL hydrocode can produce accurate
shock diffraction loading predictions for this class of problems at moderate
cost. The BRL code version has been modified to treat an incident step shock
moving obliquely through the 2-D and 3-D Cartesian grids. This allows the
modeling of the 32.75 and 34.5 kPa (nominal 5 psi) overpressure shocks striking
the front face of an S-280 Electrical Shelter at a 52.5 degree angle of
incidence, using smooth shelter walls instead of undesirable rough "stair-
stepped" surfaces formed if the shelter were rotated in the grid. The agree-
ment between the 3-D computational and experimental results is good on all
shelter faces. Errors of from -12 percent to -9 percent (H.1/E.1 and H.2/E.2,
respectively) are experienced in resolving the peak reflected overpressure on
the front face (I'2), and +7 percent to +8 percent on the windward side face
(S2); error magnitudes less than 10 percent are present beyond the peak. A
grid convergence study has quantified the sensitivity of the peak reflected
overpressure to grid size. The expected enhanced peak overpressure on the
front face at 52.5 degrees obliquity proved to be difficult to measure or
compute. It is of such short duration and limited spatial extent that it is
probably unimportant as an enhanced-damage mechanism for the S-280 Electrical
Equipment Shelter.

---

[15] H. J. Carpenter, A. L. Kuhl, and D. S. Srinivasa, "Evaluation of
Airblast Loading Prediction Techniques," AFWL-TR-80-27, US Air Force
Weapons Laboratory, Kirtland Air Force Base, NM, December 1980. (AD #B055219)

REFERENCES

1. M. A. Fry, R. E. Durrett, G. P. Ganong, D. A. Matuska, M. D. Stucker, B. S. Chambers, C. E. Needham, and C. D. Westmoreland, "The HULL Hydrodynamics Computer Code," AFWL-TR-76-183, US Air Force Weapons Laboratory, Kirtland Air Force Base, NM, September 1976. (AD #B014070L)

2. M. A. Fry, C. E. Needham, M. Stucker, B. S. Chambers, III, and G. P. Ganong, "AFWL HULL Calculations of Air Blast Over a Dam Slope," AFWL-TR-76-154, US Air Force Weapons Laboratory, Kirtland Air Force Base, NM, October 1976. (AD #B016229L)

3. J. von Neumann, "Oblique Reflection of Shocks," Bureau of Ordnance Explosive Research," Report 12, 1943.

4. H. Polacheck and R. J. Seeger, "Regular Reflection of Shocks in Ideal Gases," Bureau of Ordnance Explosives Research, Report 13, 1944.

5. L. G. Smith, "Photographic Investigation of the Reflection of Plane Shocks in Air," Office of Scientific Research and Development, Report 6271, 1945.

6. B. P. Bertrand, "Measurements of Weak Shock Wave Reflected Pressure Histories on a 2-Dimensional Surface," ARBRL-MR-02966, US Army Ballistic Research Laboratory, Aberdeen Proving Ground, Maryland, October 1979. (AD #A080539)

7. G. A. Coulter and B. P. Bertrand, "BRL Shock Tube Facility for the Simulation of Air Blast Effects," BRL-MR-1685, US Army Ballistic Research Laboratories, Aberdeen Proving Ground, MD, August 1965. (AD #475669)

8. R. E. Lottero, J. D. Wortman, B. P. Bertrand, and C. W. Kitchens, Jr., "Oblique Interaction of a Shock Wave with a Three-Dimensional Tactical Communications Shelter," Army Research Office Report 80-3, Proceedings of the 1980 Army Numerical Analysis and Computers Conference, August 1980. (AD #A089089)

9. J. A. Hasdal, B. S. Chambers, and R. W. Clemens, "Support to BRL: HULL Code Implementation on a CDC 7600," SAI-80-701-AQ, Science Applications, Inc., McLean, VA, August 1979.

10. D. C. Graham, L. P. Gaby, and C. E. Rhodes, "SAIL, An Automated Approach to Software Development and Management," AFWL Interim Report 1971-6, US Air Force Weapons Laboratory, Kirtland Air Force Base, NM, October 1976.

11. R. D. Richtmyer and K. W. Morton, Difference Methods for Initial Value Problems, Interscience Publishers, Inc., John Wiley & Sons, Inc., Second Edition, 1967.

12. R. E. Lottero, "Comparison of 3-D Hydrocode Computations for Shock
     Diffraction Loading on an S-280 Electrical Equipment Shelter," Army
     Research Office Report 80-3, Proceedings of the 1980 Army Numerical
     Analysis and Computers Conference, August 1980. (AD #A089089)

13. R. E. Lottero, "A Detailed Comparison of 3-D Hydrocode Computations
     for Shock Diffraction Loading of an S-280 Electrical Equipment Shelter,"
     ARBRL-TR-02334, US Army Ballistic Research Laboratory, Aberdeen
     Proving Ground, MD, June 1981. (AD #A102613)

14. R. A. Gentry, L. R. Stein, and C. W. Hirt, "Three-Dimensional Computer
     Analysis of Shock Loads on a Simple Structure," BRL-CR-219, US Army
     Ballistic Research Laboratory, Aberdeen Proving Ground, MD, March 1975.
     (AD #B003208L)

15. H. J. Carpenter, A. L. Kuhl, and D. S. Srinivasa, "Evaluation of
     Airblast Loading Prediction Techniques," AFWL-TR-80-27, US Air Force
     Weapons Laboratory, Kirtland Air Force Base, NM, December 1980.
     (AD #B055219)

APPENDIX A
OBLIQUE SHOCK DIFFRACTION

Figure A-1 shows a schematic view of oblique shock diffraction over a three-dimensional box-like target. Figure A-1a shows the target sitting on the ground with the line labelled "TARGET AXIS" normal to one of the faces. An incident shock is propagating toward the target, with the shock wave front perpendicular to the line labelled "SHOCK PROPAGATION AXIS," which is in turn at some general angle to the target axis. Figure A-1b shows the shock at a later time when the shock has passed part of the way across the target. The two vertical faces of the target upon which the incident shock impinges may experience different pressure loading histories, which in general depend on the shock strength and its angle of incidence.

Figure A-2 shows qualitatively the several possible wave configurations. The incident shock wave front is denoted by S, the reflected shock wave by S_R, the rarefaction wave by R, the wedge corner by C, the intersection point of either the incident shock or Mach stem with the wedge by T, and the intersection of the rarefaction wave with the wedge by A. The side of the wedge initially facing toward the shock is termed side 1, and the other side making a right angle at C is side 2. Figure A-2a shows the wave configuration when the incident shock wave strikes the wedge at normal incidence. The gas behind S is brought to rest on side 1, producing reflected shock S_R. A rarefaction wave R is generated at corner C, relieving the reflected overpressure behind S_R. On side 2, the incident shock S travels past the corner and the loading is initially unaffected by the process on side 1 until waves generated by R move around corner C and catch up to S. Figure A-2b shows the wave configuration when the wedge is tilted so that side 1 is at a slight angle to S. The intersection point T moves away from corner C at a higher speed than does point A, producing three distinct regions on side 1. The region beyond T and in front of S is ambient gas; the region between A and T has experienced only the oblique reflection of S; and the region between C and A has experienced not only the oblique reflection of S, but also the passage of rarefaction wave R. The action of S on side 2 is that of a weak oblique reflection.

Figure A-2c is conceptually the same as Figure A-2b. The angle of incidence between S and side 1 of the wedge is larger in Figure A-2c than in Figure A-2b, so the speed of T along side 1 had decreased and the distance between A and T now is growing at a slower rate than in Figure A-2b. Figure A-2d shows the situation where the angle between S and side 1 has reached the catch-up angle α_c, where the rarefaction wave R is traveling at exactly the same speed as T. In this case, the overpressure due to the shock reflection is relieved immediately for these weak shocks. Figure A-2e shows the wave configuration for an angle a few degrees larger than α_c; the reflected shock S_R is merging with the incident shock S, forming a Mach stem and a triple point at the intersection of the three shocks. The angle at which the Mach stem begins to form is denoted by α_M; it is at this angle that the peak reflected overpressure occurs.*

---

*For strong shocks, irregular Mach reflection can occur where a compression wave or shock can follow the first Mach stem.
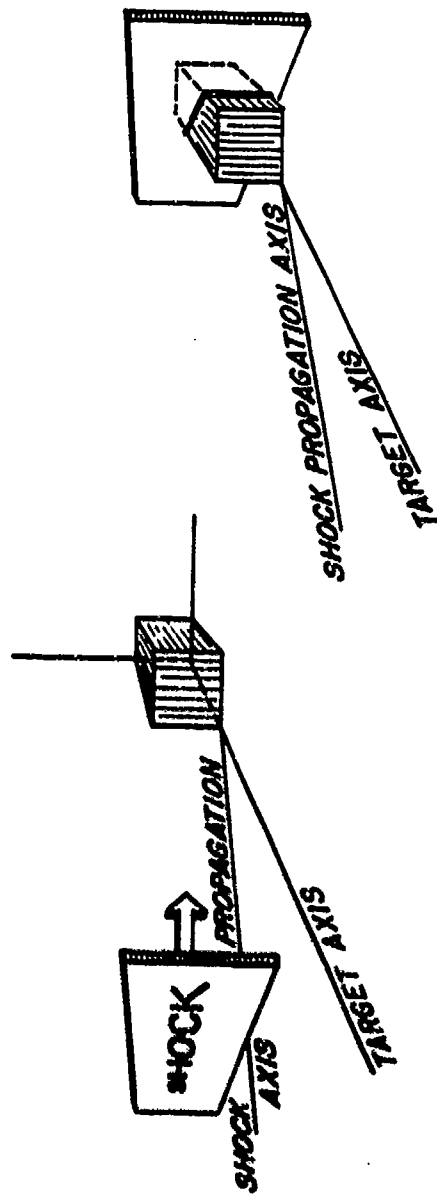
(a) Approaching shock.

(b) Diffracting shock.

Figure A-1. Three-dimensional oblique shock diffraction.

(a) Normal reflection.　(b) Regular reflection, near normal.

(c) Regular reflection, near α_C.

(d) Reflection at α_C.

(e) Mach reflection.
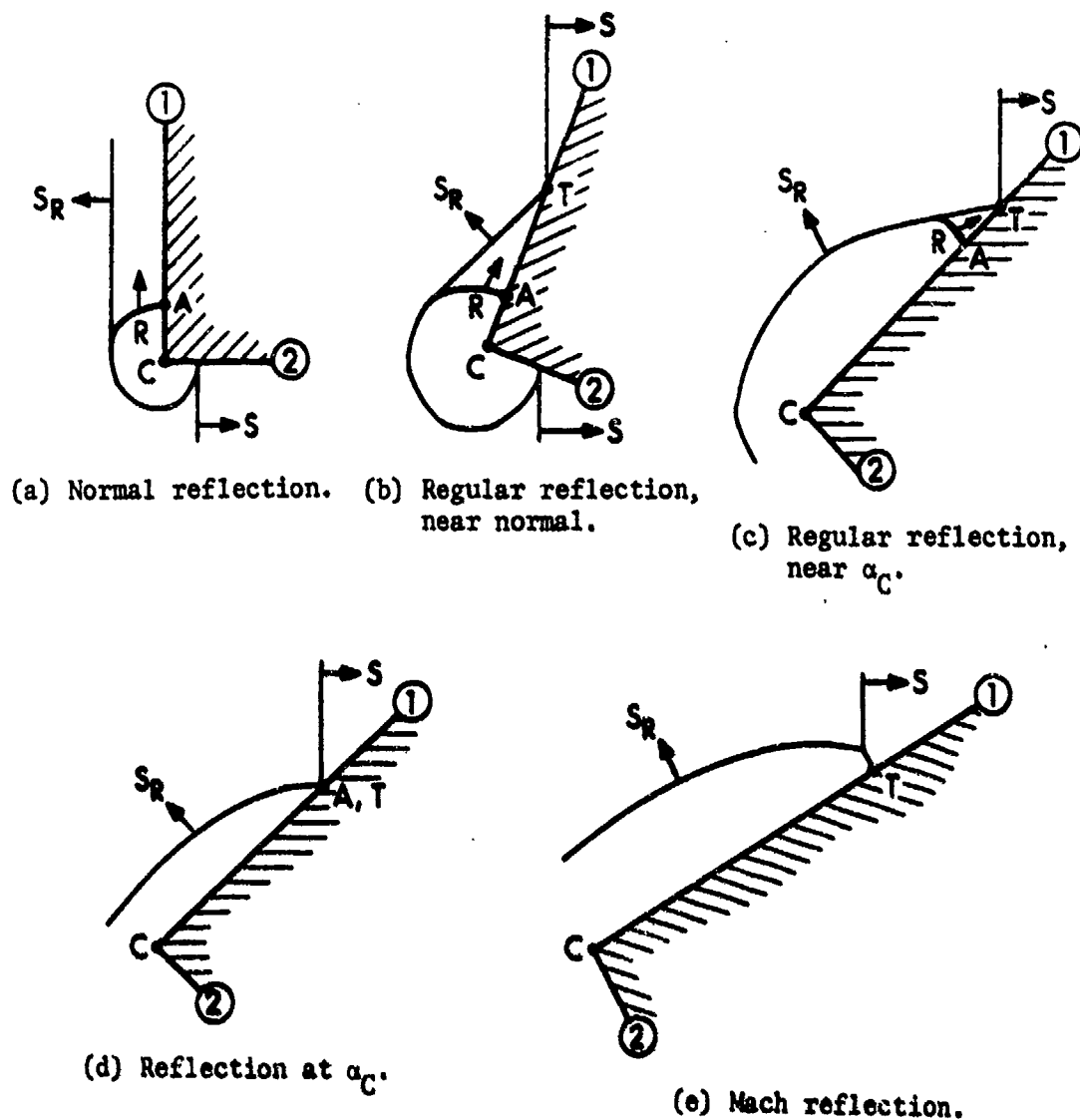
Figure A-2.　Reflected shock configurations.　(Reproduced from Reference 6.)

Figure 1 (in the main body of the report) shows the shock reflection factor (the ratio of the peak reflected overpressure to the incident over-pressure) as a function of the angle of shock incidence, α, for a 34.5 kPa (5.0 psi) overpressure incident shock wave. For this wave, which is of interest in this study, $\alpha_M = 52.5°$. The experimental data in Figure 1 were taken on a long two-dimensional wedge by Bertrand.[6] As may be seen in Figure 1, there is little change in the reflected overpressure from $\alpha = 0$ (normal reflection) to $\alpha = 36°$. Figure 1 does show that for values near $\alpha = 52.5°$, the peak overpressure for a 34.5 kPa shock is considerably larger than that for normal reflection. This peak is difficult to measure experimentally and difficult to predict computationally because of its short duration and, at least on small models, its small spatial extent. However, for large buildings such as manufacturing plants, an enhanced peak capable of causing damage may develop, hence the interest in oblique reflection of low-overpressure shocks.

APPENDIX B
ADDITIONAL INFORMATION ON EXPERIMENTS

Table B-1 shows the locations of the centers of all the pressure gage positions on the S-280 shelter model. They are given in a primed coordinate system relative to the bottom corner of the leading vertical edge of the model. The leading edge is defined as the vertical edge which the incident shock wave contacts first. The bottom corner of the leading edge is defined as (X' = 0.0, Y' = 0.0, Z' = 0.0), where X' = depth, Y' = width, and Z' = height. The primed coordinate system is defined so that the front and back faces of the model are planes of constant X'; the side faces are planes of constant Y'; and the top and bottom faces are planes of constant Z', with the bottom face at Z' = Z = 0.0. The gage positions are defined by a letter-and-number pair; the letter denotes the face and the number denotes the gage position on the face.

Table B-1. GAGE POSITIONS, COMPLETE SUMMARY

Gage Number	Face	X' (cm) (Depth)	Y' (cm) (Width)	Z' (cm) (Height)	Experiment E.1	E.2
F1	Front	0.00	17.15	5.69	No	No
F2	Front	0.00	14.68	2.84	Yes	Yes*
F3	Front	0.00	12.24	5.69	No	No
F4	Front	0.00	4.90	8.53	Yes	Yes
B1	Back	11.79	17.15	5.69	No	No
B2	Back	11.79	14.68	2.84	Yes	No
B3	Back	11.79	12.24	5.69	No	No
B4	Back	11.79	4.90	8.53	Yes	Yes
S1	Leeward Side	5.89	19.58	5.69	Yes	Yes
S2	Windward Side	5.89	0.00	5.69	Yes	Yes
T1	Top	5.89	14.68	11.38	Yes	Yes
T2	Top	5.89	4.90	11.38	Yes	Yes

*High frequency response ST-4-116 gage

All gages, except for the gage at position F2 for shot E.2 were PcB Model 113A24 gages, with a frequency response of 500 kHz and a sensitive element diameter of 0.51 cm (0.20 in). The gage at position F2 for shot E.2 was a Susquehanna Instruments Model ST-4-116 gage, with a frequency response of 2.0 MHz and a sensitive element diameter of 0.16 cm (0.063 in).

The output from the PcB pressure gages was recorded on magnetic tape. The tape recorder has an 80 kHz bandwidth, which provides a response to a square-wave input signal to within 4 percent in 10 μs and 1 percent in 25 μs. Thus, the response of this measuring system was limited by the tape recorder's characteristics rather than by the gage response. The digitizing rate for these data was one datum every 2.5 μs.

The output from the ST-4-116 gage was recorded on both magnetic tape and an oscilloscope. The response of the ST-4-116/oscilloscope recording was limited by the time it takes the shock to cross the gage. The ST-4-116/ oscilloscope combination was used to obtain data as close in time as possible to the passage of the shock front.

The digitized data were analyzed and stored on the BRL CDC 173 for later comparison with the hydrocode computations.

APPENDIX C
COMPUTATIONAL GRIDS

LIST OF TABLES

I.   COMPUTATIONS H.1 AND H.2

The finite difference grids used for 3-D computations H.1 and H.2 (see Table 3) are identical. Each contains 92,512 flow field cells, with 49 cells in the X direction (depth), 59 cells in the Y direction (width), and 32 cells in the Z direction (height). The target is modeled using 6,912 nearly-cubical rigid cells, with 16 equal X-direction cells ($\Delta X = 0.7366$ cm), 27 equal Y-direction cells ($\Delta Y = 0.7253$ cm), and 16 equal Z-direction cells ($\Delta Z = 0.7112$ cm). The rigid cells do not directly enter into the computation other than to provide a non-responding, perfect-reflection structure in the flow field. To conserve storage space in the computer and yet have the boundaries of the computational grid as far removed as practical from the shelter, cell sizes moving away from the shelter are increased using geometric progression factors of 1.07 (or less) for cell-to-cell size increases. Cell vertex locations are shown in Table C-1.

Figure C-1 shows a top view of the initial shock location in the hydro-code grid. The shock is denoted by line DE, where E is its intersection point with the X axis and D is its intersection point with the Y axis. The axes' origin is denoted by point P. The shock velocity vector is parallel to line PB, which is perpendicular to the shock front DE. The leading corner of the shelter is denoted by point A, and the angle of obliquity, α, between the shock and the shelter front face is 52.5 degrees. Line AC is parallel to DE; line BC, the initial distance of the shock from the shelter corner A, is 2.6551 cm.

II.   COMPUTATION H.3

The high-resolution finite-difference grid used for the 3-D computation H.3 is a modified version of that used for computations H.1 and H.2. The cell sizes have been reduced by a factor of 2 in each direction. The X = 0.0 and Y = 0.0 grid boundaries have been moved closer to the shelter model. The $X = X_{max}$, $Y = Y_{max}$ and $Z = Z_{max}$ boundaries have been moved in past the respective ends of the shelter model, so that not all of the shelter is modeled in the grid. The regions of primary interest on the shelter were those near the simulated gage positions F2 and S2. The grid was designed so that enough computational time was simulated to compute the peak overpressures at these points. The grid reduction was necessary to keep computing time within acceptable levels. (Halving cell sizes in a 3-D grid for an explicit-time-step code increases computer time by a factor of 2^4, all other things being equal.)

The finite difference grid contains 32,850 flow field cells, with 45 cells in the X direction, 73 cells in the Y direction, and 10 cells in the Z direction. The partial shelter model is built using 12,190 nearly cubical rigid cells, with 23 equal X-direction cells ($\Delta X = 0.3683$ cm), 53 equal Y-direction cells ($\Delta Y = 0.36265$ cm), and 10 equal Z-direction cells ($\Delta Z = 0.3556$ cm). The cell sizes for the grid are shown in Table C-2.

49

TABLE C-1. CELL DIMENSIONS FOR COMPUTATIONS H.1 AND H.2

	Cell Dimensions (cm)		
Index	Depth, I Index	Width, J Index	Height, K Index
1	1.7521	1.9634	.7112*
2	1.6598	1.8373	.7112*
3	1.5723	1.7192	.7112*
4	1.4984	1.6088	.7112*
5	1.4109	1.5055	.7112*
6	1.3365	1.4088	.7112*
7	1.2660	1.3183	.7112*
8	1.1993	1.2336	.7112*
9	1.1361	1.1544	.7112*
10	1.0762	1.0802	.7112*
11	1.0194	1.0108	.7112*
12	.9657	.9459	.7112*
13	.9148	.8851	.7112*
14	.8666	.8283	.7112*
15	.8209	.7751	.7112*
16	.7776	.7253	.7112*
17	.7366	.7253*	.7712
18	.7366*	.7253*	.7617
19	.7366*	.7253*	.8158
20	.7366*	.7253	.8737
(Continued)			

* Rigid cell within computational shelter model

50

TABLE C-1. CELL DIMENSIONS FOR COMPUTATIONS
H.1 and H.2 (Continued)

Index	Cell Dimensions (cm)		
	Depth, I Index	Width, J Index	Height, K Index
21	.7366*	.7253*	.9357
22	.7366*	.7253*	1.0022
23	.7366*	.7253*	1.0733
24	.7366*	.7253*	1.1495
25	.7366*	.7253*	1.2311
26	.7366*	.7253*	1.3186
27	.7366*	.7253*	1.4122
28	.7366*	.7253*	1.5124
29	.7366*	.7253*	1.6198
30	.7366*	.7253*	1.7348
31	.7366*	.7253*	1.8580
32	.7366*	.7253*	1.9899
33	.7366*	.7253*	
34	.7366	.7253*	
35	.7858	.7253*	
36	.8383	.7253*	
37	.8942	.7253*	
38	.9540	.7253*	
39	1.0177	.7253*	
40	1.0856	.7253*	
(Continued)			

*Rigid cell within computational shelter model

51

TABLE C-1. CELL DIMENSIONS FOR COMPUTATIONS
H.1 AND H.2 (Continued)

Index	Cell Dimensions (cm)		
	Depth, I Index	Width, J Index	Height, K Index
41	1.5181	.7253*	
42	1.2355	.7253*	
43	1.3180	.7253*	
44	1.4060	.7253	
45	1.4999	.7751	
46	1.6001	.8283	
47	1.7069	.8851	
48	1.8202	.9459	
49	1.9425	1.0108	
50		1.0802	
51		1.1544	
52		1.2336	
53		1.3183	
54		1.4088	
55		1.5055	
56		1.6088	
57		1.7192	
58		1.8373	
59		1.9634	

*Rigid cell within computational shelter model

Figure C-1. Initial shock location, top view.

TABLE C-2.   CELL DIMENSIONS FOR COMPUTATION H.3

Index	Cell Dimensions (cm)		
	Depth, I Index	Width, J Index	Height, K Index
1	.63300	.65915	.35560*
2	.63300	.65915	.35560*
3	.59965	.61680	.35560*
4	.59965	.61680	.35560*
5	.56805	.57720	.35560*
6	.56805	.57720	.35560*
7	.53810	.54010	.35560*
8	.53810	.54010	.35560*
9	.50970	.50540	.35560*
10	.50970	.50540	.35560*
11	.48285	.47295	
12	.48285	.47295	
13	.45740	.44255	
14	.45740	.44255	
15	.43330	.41415	
16	.43330	.41415	
17	.41045	.38755	
18	.41045	.38755	
19	.38880	.36265	
20	.38880	.36265	
21	.36830	.36265*	
22	.36830	.36265*	
23 - 45	.36830*	.36265*	
46 - 73		.36265*	

*Rigid cell within computational shelter model.

Because the partial shelter model extends from the bottom to the top of the grid, this computation does not model rarefaction waves which would normally move from the top of a face to the bottom. However, the desired simulated time is short enough that these waves do not arrive at F2 and S2 until well after the peak overpressure occurs at those points.

III. COMPUTATION H.4

The finite difference grid used for 2-D computation H.4 is a 2-D slice of the grid for computations H.1 and H.2, taken at the ground level (K = 1) plane. The columns for the I and J index cell sizes in Table C-1 are those for the computational grid for H.4, having 49 cells in the X direction, and 59 cells in the Y direction.

IV. COMPUTATION H.5

The finite difference grid used for computation H.5 has twice the resolution (i.e., 50 percent smaller computational cell sizes in each direction) of computation H.4. As was done for 3-D computation H.2, a portion of the rigid shelter was placed in the upper right corner of the grid (the high I and J index region). Enough of the shelter was modeled so that reliable computations for the pressure peaks at positions F2 and S2 were possible. The computational cell sizes are shown in Table C-3. The cell sizes at the rigid shelter are $\Delta X = 0.36830$ cm and $\Delta Y = 0.36265$ cm.

V. COMPUTATION H.6

The finite difference grid used for computation H.6 has twice the resolution of computation H.5, and four times that of H.4. Its configuration is similar to that for H.5. The computational cell sizes are shown in Table C-4. The cell sizes at the rigid shelter are $\Delta X = 0.18415$ cm and $\Delta Y = 0.181325$ cm.

VI. COMPUTATION H.7

The finite difference grid for computation H.7 has twice the resolution of computation H.6, and eight times that of H.4. Its configuration is similar to those of H.5 and H.6, except that the boundaries have been moved in closer. The computational cell sizes are shown in Table C-5. The cell sizes at the rigid shelter are $\Delta X = 0.092075$ cm and $\Delta Y = 0.0906625$ cm.

TABLE C-3. CELL DIMENSIONS FOR COMPUTATION H.5

| Index | Cell Dimensions (cm) | |
	Depth, I Index	Width, J Index
1 - 6	.77460	.96400
7	.77460	.96315
8	.77460	.94000
9	.77460	.89000
10	.77460	.85000
11	.77460	.80900
12	.77460	.76900
13	.77460	.73200
14	.77520	.69600
15	.74600	.66200
16	.70900	.62900
17	.67500	.59900
18	.64100	.56900
19	.61000	.54200
20	.58000	.51500
21	.55100	.48800
22	.52400	.46600
23	.49800	.44300
24	.47400	.42100
25	.45100	.40109
26	.42900	.38125
27	.40700	.36265
28	.38700	.36265
29 - 30	.36830	.36265
31 - 32	.36830	.36265*
33 - 64	.36830*	.36265*
65 - 84		.36265*

*Rigid cell within computational shelter model.

56

TABLE C-4. CELL DIMENSIONS FOR COMPUTATION H.6

| Index | Cell Dimensions (cm) | |
	Depth, I Index	Width, J Index
1 - 2	.553125	.633575
3 - 4	.553125	.605
5 - 6	.553125	.575
7 - 8	.553125	.545
9 - 10	.53	.52
11 - 12	.505	.495
13 - 14	.48	.47
15 - 16	.455	.445
17 - 18	.435	.425
19 - 20	.4125	.4045
21 - 22	.3925	.3845
23 - 24	.373	.366
25 - 26	.3545	.348
27 - 28	.3375	.331
29 - 30	.3205	.3145
31 - 32	.305	.2995
33 - 34	.29	.2845
35 - 36	.2755	.271
37 - 38	.262	.2575
39 - 40	.249	.244
41 - 42	.237	.233
43 - 44	.2255	.2215
45 - 46	.2145	.2105
47 - 48	.2035	.2005
49 - 50	.1935	.190625
51 - 58	.18415	.181325
59 - 122	.18415*	.181325*
123 - 166		.181325*

*Rigid cell within computational shelter model.

57

TABLE C-5.   CELL DIMENSIONS FOR COMPUTATION H.7

| Index | Cell Dimensions (cm) | |
	Depth, I Index	Width J Index
1	.508375	.5150125
2	.4854	.4908
3	.4628	.4671
4	.4414	.4451
5	.4209	.4242
6	.4014	.4042
7	.3828	.3852
8	.3650	.3670
9	.3481	.3498
10	.3319	.3333
11	.3165	.3176
12	.3019	.3027
13	.2879	.2884
14	.2745	.2748
15	.2618	.2619
16	.2496	.2496
17	.2381	.2378
18	.2270	.2266
19	.2165	.2160
20	.2064	.2058
21	.1969	.1961
22	.1877	.1869
23	.1790	.1781
24	.1707	.1697
25	.1628	.1617
(Continued)		

TABLE C-5. CELL DIMENSIONS FOR
COMPUTATION H.7 (Continued)

Index	Cell Dimensions (cm)	
	Depth, I Index	Width, J Index
26	.1553	.1541
27	.1480	.1468
28	.1412	.1399
29	.1346	.1333
30	.1284	.1271
31	.1224	.1211
32	.1168	.1154
33	.1113	.1099
34	.1062	.1048
35	.1012	.0998
36	.0966	.0951
37 - 47	.092075	.0906625
48 - 132	.092075*	.0906625*
133 - 260		.0906625*

*Rigid cell within computational shelter model.

DISTRIBUTION LIST

No. of Copies	Organization	No. of Copies	Organization
12	Administrator Defense Technical Info Center ATTN: DTIC-DDA Cameron Station Alexandria, VA 22314	1	Director Defense Communications Agency ATTN: 930 Washington, DC 20305
1	Director of Defense Research & Engineering ATTN: DD/TWP Washington, DC 20301	3	Director Defense Nuclear Agency ATTN: DDST TIPL/Tech Lib SPSS/K. Goering G. Ullrich SPTD/T. Kennedy SPAS STSP NATD NATA Washington, DC 20305
1	Asst. to the Secretary of Defense (Atomic Energy) ATTN: Document Control Washington, DC 20301		
1	Director Defense Advanced Research Projects Agency ATTN: Tech Lib 1400 Wilson Boulevard Arlington, VA 22209		
2	Director Federal Emergency Management Agency ATTN: Mr. George Sisson/RF-SR Technical Library Washington, DC 20301	2	Commander Field Command, DNA ATTN: FCPR FCTMOF Kirtland AFB, NM 87115
1	Director Defense Intelligence Agency ATTN: DT-2/Wpns & Sys Div Washington, DC 20301	1	Commander Field Command, DNA Livermore Branch ATTN: FCPRL P.O. Box L-395 Livermore, CA 94550
1	Director National Security Agency ATTN: E. F. Butala, R15 Ft. George G. Meade, MD 20735	1	Director Inst for Defense Analyses ATTN: IDA Librarian, Ruth S. Smith 1801 Beauregard St. Alexandria, VA 22311
1	Director Joint Strategic Target Planning Staff JCS Offut AFB Omaha, NB 68113	1	Director US Army BMD Program Office ATTN: John Shea 5001 Eisenhower Avenue Alexandria, VA 22333

61

DISTRIBUTION LIST

No. of Copies	Organization	No. of Copies	Organization

2	Director
	US Army BMD Advanced
	  Technology Center
	ATTN: CRDABH-X
	      CRDABH-S
	Huntsville, AL 35804
		1	Commander
			US Army Materiel Development
			  and Readiness Command
			ATTN: DRCDMD-ST
			5001 Eisenhower Avenue
			Alexandria, VA 22333

1	Commander US Army BMD Command ATTN: BDMSC-TFN/N.J. Hurst P.O. Box 1500 Huntsville, AL 35804	1	Commander US Army Armament Research and Development Command ATTN: DRDAR-TDC Dover, NJ 07801

2	Deputy Chief of Staff for
	  Operations and Plans
	ATTN: Technical Library
	      Director of Chemical
	        & Nuc Operations
	Department of the Army
	Washington, DC 20310
		3	Commander
			US Army Armament Research
			  and Development Command
			ATTN: DRDAR-LCN-F, W. Reiner
			      DRDAR-TSS (2 cys)
			Dover, NJ 07801

2	Office, Chief of Engineers
	Department of the Army
	ATTN: DAEN-MCE-D
	      DAEN-RDM
	890 South Pickett Street
	Alexandria, VA 22304
		1	Commander
			US Army Armament Materiel
			  Readiness Command
			ATTN: DRSAR-LEP-L, Tech Lib
			Rock Island, IL 61299

3	Commander
	US Army Engineer
	Waterways Experiment Station
	ATTN: Technical Library
	      William Flathau
	      Leo Ingram
	P.O. Box 631
	Vicksburg, MS 39181
		1	Director
			US Army ARRADCOM
			Benet Weapons Laboratory
			ATTN: DRDAR-LCB-TL
			Watervliet, NY 12189

1	Commander US Army Engineer School ATTN: ATSEN-SY-L Fort Belvoir, VA 22060	1	Commander US Army Aviation Research and Development Command ATTN: DRDAV-E 4300 Goodfellow Boulevard St. Louis, MO 63120
1	US Army MERADCOM ATTN: DRDME-EM, D. Frink Fort Belvoir, VA 22060	1	Director US Army Air Mobility Research and Development Laboratory Ames Research Center Moffett Field, CA 94035

DISTRIBUTION LIST

No. of Copies	Organization	No. of Copies	Organization
1	Commander US Army Communications Rsch and Development Command ATTN: DRDCO-PPA-SA Fort Monmouth, NJ 07703	4	Commander US Army Natick Research and Development Command ATTN: DRDNA/Dr. Sieling DRXNE-UE/A. Johnson A. Murphy W. Crenshaw Natick, MA 01762
3	Commander US Army Electronics Research and Development Command ATTN: DELSD-L DELEW-E, W. S. McAfee DELSD-EI, J. Roma Fort Monmouth, NJ 07703	1	Commander US Army Tank Automotive Rsch and Development Command ATTN: DRDTA-UL Warren, MI 48090
8	Commander US Army Harry Diamond Labs ATTN: Mr. James Gaul Mr. L. Belliveau Mr. J. Meszaros Mr. J. Gwaltney Mr. F. W. Balicki Mr. Bill Vault Mr. R. J. Bostak Mr. R. K. Warner 2800 Powder Mill Road Adelphi, MD 20783	1	Commander US Army Foreign Science and Technology Center ATTN: Rsch & Concepts Br 220 7th Street, NE Charlottesville, VA 22901
4	Commander US Army Harry Diamond Labs ATTN: DELHD-TA-L DRXDO-TI/002 DRXDO-NP DELHD-RBA/J. Rosado 2800 Powder Mill Road Adelphi, MD 20783	1	Commander US Army Logistical Center ATTN: ATCL-SCA Mr. Robert Cameron Fort Lee, VA 23801
1	Commander US Army Missile Command ATTN: DRSMI-R Redstone Arsenal, AL 35898	3	Commander US Army Materials and Mechanics Research Center ATTN: Technical Library DRXMR-ER, Joe Prifti Eugene de Luca Watertown, MA 02172
1	Commander US Army Missile Command ATTN: DRSMI-YDL Redstone Arsenal, AL 35898	1	Commander US Army Research Office P.O. Box 12211 Research Triangle Park NC 27709
1	Commander US Army Missile Command ATTN: Technical Library Redstone Arsenal, AL 35898	4	Commander US Army Nuclear & Chemical Agency ATTN: ACTA-NAW MONA-WE Technical Library MAJ Uecke 7500 Backlick Rd, Bldg. 2073 Springfield, VA 22150

DISTRIBUTION LIST

No. of Copies	Organization	No. of Copies	Organization
1	Commander US Army TRADOC ATTN: ATCD-SA Fort Monroe, VA 23651	1	Commander Naval Electronic Systems Com ATTN: PME 117-21A Washington, DC 20360

2	Director
	US Army TRADOC Systems
	  Analysis Activity
	ATTN: LTC John Hesse
	      ATAA-SL, Tech Lib
	White Sands Missile Range
	NM 88002
		1	Commander
			Naval Facilities Engineering
			  Command
			ATTN: Technical Library
			Washington, DC 20360

1	Commander US Combined Arms Combat Developments Activity ATTN: ATCA-CO, Mr. L. C. Pleger Fort Leavenworth, KS 66027	1	Commander Naval Sea Systems Command ATTN: ORD-91313 Library Department of the Navy Washington, DC 20362

1	Commandant
	Interservice Nuclear Weapons
	  School
	ATTN: Technical Library
	Kirtland AFB, NM 87115
		3	Officer-in-Charge (Code L31)
			Civil Engineering Laboratory
			Naval Constr Btn Ctr
			ATTN: Stan Takahashi
			      R. J. Odello
			      Technical Library
			Port Hueneme, CA 93041

1	Chief of Naval Material ATTN: MAT 0323 Department of the Navy Arlington, VA 22217	1	Commander David W. Taylor Naval Ship Research & Development Ctr ATTN: Lib Div, Code 522 Bethesda, MD 20084
2	Chief of Naval Operations ATTN: OP-03EG OP-985F Department of the Navy Washington, DC 20350	1	Commander Naval Surface Weapons Center ATTN: DX-21, Library Br. Dahlgren, VA 22448

1	Chief of Naval Research
	ATTN: N. Perrone
	Department of the Navy
	Washington, DC 20360
		2	Commander
			Naval Surface Weapons Center
			ATTN: Code WA501/Navy Nuclear
			         Programs Office
			         Code WX21/Tech Lib
			Silver Spring, MD 20910

1	Director Strategic Systems Projects Ofc ATTN: NSP-43, Tech Lib Department of the Navy Washington, DC 20360	1	Commander Naval Weapons Center ATTN: Code 533, Tech Lib China Lake, CA 93555

DISTRIBUTION LIST

No. of Copies	Organization	No. of Copies	Organization
1	Commander Naval Weapons Evaluation Fac ATTN: Document Control Kirtland Air Force Base Albuquerque, NM 87117	1	Director Lawrence Livermore Lab ATTN: Tech Info Dept L-3 P.O. Box 808 Livermore, CA 94550
1	Commander Naval Research Laboratory ATTN: Code 2027, Tech Lib Washington, DC 20375	2	Director Los Alamos Scientific Lab ATTN: Doc Control for Rpts Lib R. A. Gentry P.O. Box 1663 Los Alamos, NM 87544
1	Superintendent Naval Postgraduate School ATTN: Code 2124, Technical Reports Library Monterey, CA 93940	2	Sandia Laboratories ATTN: Doc Control for 3141 Sandia Rpt Collection L. J. Vortman Albuquerque, NM 87115
1	AFSC (Tech Lib) Andrews Air Force Base Washington, DC 20331		
1	ADTC (DLODL) Eglin AFB, FL 32542	1	Sandia Laboratories Livermore Laboratory ATTN: Doc Control for Tech Lib P.O. Box 969 Livermore, CA 94550
1	AFATL (DLYV) Eglin AFB, FL 32542	1	Director National Aeronautics and Space Administration Scientific & Tech Info Fac P.O. Box 8757 Baltimore/Washington International Airport MD 21240
1	RADC (EMTLD/Docu Library) Griffiss AFB, NY 13440		
1	AFWL/NTES (R. Henny) Kirtland AFB, NM 87115		
1	AFWL/NTE, CPT J. Clifford Kirtland AFB, NM 87115		
2	Commander-in-Chief Strategic Air Command ATTN: NRI-STINFO Lib Offutt AFB, NB 68113	1	Aerospace Corporation ATTN: Tech Info Services P.O. Box 92957 Los Angeles, CA 90009
1	AFIT (Lib Bldg. 640, Area B) Wright-Patterson AFB Ohio 45433	1	Agbabian Associates ATTN: M. Agbabian 250 North Nash Street El Segundo, CA 90245
1	FTD (FTO/NIIS) Wright-Patterson AFB Ohio 45433		

65

DISTRIBUTION LIST

No. of Copies	Organization
1	The BDM Corporation ATTN: Richard Hensley P.O. Box 9274 Albuquerque International Albuquerque, NM 87119
1	The Boeing Company ATTN: Aerospace Library P.O. Box 3707 Seatle, WA 98124
1	Goodyear Aerospace Corp ATTN: R. M. Brown, Bldg 1 Shelter Engineering Litchfield Park, AZ 85340
5	Kaman AviDyne ATTN: Dr. N.P. Hobbs (4 cys) Mr. S. Criscione 83 Second Avenue Northwest Industrial Park Burlington, MA 01830
3	Kaman Sciences Corporation ATTN: Library P. A. Ellis F. H. Shelton 1500 Garden of the Gods Road Colorado Springs, CO 80907
1	Kaman Sciences Corporation ATTN: Don Sachs Suite 703 2001 Jefferson Davis Highway Arlington, VA 22202
1	Kaman-TEMPO ATTN: DASIAC P.O. Drawer QQ Santa Barbara, CA 93102
1	Kaman-TEMPO ATTN: E. Bryant, Suite UL-1 715 Shamrock Road Bel Air, MD 21014

No. of Copies	Organization
1	Lockheed Missiles & Space Co. ATTN: J. J. Murphy, Dept. 81-11 Bldg. 154 P.O. Box 504 Sunnyvale, CA 94086
1	Martin Marietta Aerospace Orlando Division ATTN: G. Fotieo P.O. Box 5837 Orlando, FL 32805
2	McDonnell Douglas Astronautics Corporation ATTN: Robert W. Halprin Dr. P. Lewis 5301 Bolsa Avenue Huntington Beach, CA 92647
2	The Mitre Corporation ATTN: Library J. Calligeros, Mail Stop B-150 P.O. Box 208 Bedford, MA 01730
1	Pacific Sierra Research Corp ATTN: Dr. Harold Brode 1456 Cloverfield Boulevard Santa Monica, CA 90404
1	Physics International Corp 2700 Merced Street San Leandro, CA 94577
1	Radkowski Associates ATTN: Peter R. Radkowski P.O. Box 5474 Riverside, CA 92517
4	R&D Associates ATTN: Jerry Carpenter J. G. Lewis Technical Library Allan Kuhl P.O. Box 9695 Marina del Rey, CA 90291

DISTRIBUTION LIST

No. of Copies	Organization	No. of Copies	Organization
1	RCA Government Communications Systems 13-5-2 Front & Cooper Streets Camden, NJ 08102	1	California Inst of Tech ATTN: T. J. Ahrens 1201 E. California Blvd. Pasadena, CA 91109
2	Science Applications, Inc. ATTN: Burton S. Chambers John Cockayne P.O. Box 1303 1710 Goodridge Drive McLean, VA 22102	2	University of Denver Denver Research Institute ATTN: Mr. J. Wisotski Technical Library P.O. Box 10127 Denver, CO 80210
1	Science Applications, Inc. ATTN: Technical Library P.O. Box 2351 La Jolla, CA 92038	1	IIT Research Institute ATTN: Milton R. Johnson 10 West 35th Street Chicago, IL 60616
1	Systems Science & Software ATTN: C. E. Needham P.O. Box 8243 Albuquerque, NM 87198	1	J. D. Haltiwanger Consulting Services B106a Civil Engineering Bldg. 208 N. Romine Street Urbana, IL 61801
1	Systems Science & Software ATTN: Technical Library P.O. Box 1620 La Jolla, CA 92037	1	Massachusetts Institute of Technology Aeroelastic and Structures Research Laboratory ATTN: Dr. E. A. Witmer Cambridge, MA 02139
1	TRW Systems Group ATTN: Benjamin Sussholtz One Space Park Redondo Beach, CA 90278	2	Southwest Research Institute ATTN: Dr. W. E. Baker A. B. Wenzel 8500 Culebra Road San Antonio, TX 78206
2	Union Carbide Corporation Holifield National Laboratory ATTN: Doc Control for Tech Lib Civil Defense Research Proj P.O. Box X Oak Ridge, TN 37830	1	SRI International ATTN: Dr. G. R. Abrahamson 333 Ravenswood Avenue Menlo Park, CA 94025
1	Weidlinger Assoc. Consulting Engineers ATTN: M. L. Baron 110 East 59th Street New York, NY 10022	1	Stanford University ATTN: Dr. D. Bershader Durand Laboratory Stanford, CA 94305
1	Battelle Memorial Institute ATTN: Technical Library 505 King Avenue Columbus, OH 43201		

67

DISTRIBUTION LIST

No. of
Copies   Organization

1   Washington State University
    Physics Department
    ATTN: G. R. Fowles
    Pullman, WA   99164

Aberdeen Proving Ground

Dir, USAMSAA
    ATTN: DRXSY-D
           DRXSY-MP, H. Cohen
Cdr, USATECOM
    ATTN: DRSTE-TO-F
Dir, USACSL
    Bldg. E3516, EA
      ATTN: DRDAR-CLB-PA